List of Publications

Published

- Ruchika, **Khan. N,** Saneja. A*. **(2024)** The Dawning Era of Oral Thin Films for Nutraceutical Delivery: From Laboratory to Clinic, **Biotechnology Advances**, 73, 108362, **https://doi.org/10.1016/j.biotechadv.2024.108362 (IF: 12.10)**

- **Khan. N,** Slathia. G, Saneja. A, * **(2023)**. Unveiling the complexation mechanism of phloretin with Sulfobutylether–β–cyclodextrin (Captisol®) and its impact on anticancer activity, **Journal of Molecular Liquids**, 391 (part B), 123348. **https://doi.org/10.1016/j.molliq.2023.123348 (IF: 5.30)**

- **Khan. N,** Slathia. G, Kaliya. K, Saneja. A*. **(2023)**. Recent progress in covalent organic frameworks for cancer therapy, **Drug Discovery Today**, 28, 103602, **https://doi.org/10.1016/j.drudis.2023 (IF: 6.50)**

- **Khan. N,** A.K. Singh, Saneja A., * **(2023) "**Preparation, Characterization, and Antioxidant Activity of L-Ascorbic Acid/HP-β-Cyclodextrin Inclusion Complex-Incorporated Electro-spun Nanofibers, **Foods**, 12(7), 1363, **https://doi.org/10.3390/foods12071363 (IF: 4.70)**

- **Khan. N,** Bhardwaj V.K., Ruchika, Purohit R. *, Saneja A. * **(2023)**. Deciphering the interactions of genistein with *β*-cyclodextrin derivatives through experimental and microsecond timescale umbrella sampling simulations. **Journal of Molecular Liquids**, 374, 121295. **https://doi.org/10.1016/j.molliq.2023.121295 (IF: 5.30)**

- **Khan. N,** Ruchika, Dhritlahre, R. K., Saneja. A*. **(2022)** "Recent advances in dual-ligand targeted nanocarriers for cancer therapy". **Drug Discovery Today**, 27, 2288-2299. **https://doi.org/10.1016/j.drudis.2022.04.011 (IF: 6.50)**

- Ahirwar. R*, **Khan. N,** Kumar. S. **(2021)** "Aptamer-based sensing of breast cancer biomarkers: a comprehensive review of analytical figures of merit". **Expert Review of Molecular Diagnostics,** 21 (7), 703-721, **https://doi.org/10.1080/14737159.2021.1920397 (IF: 3.90)**

- Rawat A.B., **Khan. N,** Singh S.K., Patil U.K.*, (2023) "Delayed Release HPMC Capsules for Efficient Delivery of Cholecalciferol Solid Dispersion, **Indian journal of Pharmaceutical Education and Research**, **DOI: 10.5530/ijper.57.2.51**

Under preparation/communication:

- **Khan. N**, Saneja A.* (2024). “Colon Targeted Delivery of Quercetin from Sulfobutylether-β-Cyclodextrin Inclusion Complex Incorporated Electrospun Eudragit® S100 Nanofibers” (Under preparation).

- **Khan. N**, Saneja A.* (2024). “Inclusion Complex of Naringenin with Sulfobutylether-β-cyclodextrin derivative: Characterizations, antioxidant and antibacterial activity” (Under preparation).

- **Khan. N**, Saneja A.* (2024). “Formononetin loaded cyclodextrin nanosponges: Preparation, characterizations and antibacterial activity” (Under preparation).

Published Book Chapters

- Ahirwar. R*, **Khan. N. (2022)** “Smart wireless nanosensor system for human healthcare”. **Nanosensors for Futuristic Smart and Intelligent Healthcare Systems** (1st Edition). Eds by Suresh Kaushik, Vijay Soni, Efstathia Skotti. 265-288. (Publisher: CRC Press)
- Ahirwar. R*, **Khan. N. (2024) “**Aptamer-based point-of-care testing: an overview from past to future”. **Aptasensors for Point-of-Care Diagnostics of Cancer: From lab to clinics**. https://doi.org/10.1088/978-0-7503-5012-9ch1. 1-19 (IOP Science publishing)

Journal of Molecular Liquids 374 (2023) 121295

Contents lists available at ScienceDirect

Journal of Molecular Liquids

journal homepage: www.elsevier.com/locate/molliq

Deciphering the interactions of genistein with β-cyclodextrin derivatives through experimental and microsecond timescale umbrella sampling simulations

Nabab Khan [a,d], Vijay Kumar Bhardwaj [b,c,d], Ruchika [a,d], Rituraj Purohit [b,c,d,*], Ankit Saneja [a,d,*]

[a] Formulation Laboratory, Dietetics and Nutrition Technology Division, CSIR-Institute of Himalayan Bioresource Technology, Palampur 176061, Himachal Pradesh, India
[b] Structural Bioinformatics Laboratory, CSIR-Institute of Himalayan Bioresource Technology, Palampur 176061, Himachal Pradesh, India
[c] Biotechnology Division, CSIR-IHBT, Palampur 176061, Himachal Pradesh, India
[d] Academy of Scientific and Innovative Research (AcSIR), Ghaziabad 201002, Uttar Pradesh, India

ARTICLE INFO

Article history:
Received 18 September 2022
Revised 2 January 2023
Accepted 18 January 2023
Available online 21 January 2023

Keywords:
Genistein
Cyclodextrin
Spectroscopy
Interaction
Gibbs free energy potential
Umbrella sampling

ABSTRACT

Genistein (GEN), an isoflavone, exhibits wide array of biological activities such as antioxidant, anti-inflammatory, cardioprotective and neuroprotective effects. However, despite of tremendous biological activities, its incorporation into functional foods and food supplements is limited due to its low aqueous solubility and instability. The present investigation unveils the molecular mechanism of inclusion of GEN inside the cyclodextrins (CDs) cavities with special emphasis on the correlation of experimental methods with molecular dynamics (MD) simulations. Herein, host – guest inclusion complexes (ICs) of GEN with two modified forms of β-cyclodextrins [Methyl-β-cyclodextrin (M-β-CD) & Hydroxypropyl-β-cyclodextrin (HP-β-CD)] were prepared using spray-drying to improve the aqueous solubility and the apparent stability of GEN. The ICs were characterized by fourier transform infra-red (FT-IR) spectroscopy, powder X-ray diffractometry (PXRD), scanning electron microscopy (SEM) and nuclear magnetic resonance spectroscopy (^{1}H NMR and 2D-NOESY) providing appropriate evidences of the inclusion of GEN inside host cavities (CDs). The results of MD simulations demonstrated multiple conformations obtaining energy minimas of GEN/M-β-CD, whereas GEN/HP-β-CD only showed a single metastable structure. The results were further complemented by enhanced umbrella sampling simulations where GEN/M-β-CD demonstrated lower free energy of binding than GEN/HP-β-CD. Overall, this study presents basic mechanism behind GEN/CD inclusion complexes formation using experimental and computational approaches.

1. Introduction

Nutraceuticals have gained tremendous attention in the past decade because of their wide array of therapeutic and preventive effects [1]. In this regard, genistein (GEN) [5,7-dihyroxy-3-(-4-hydroxyphenyl)-4H-1-benzopyran-4-one], one of the abundant isoflavone in soybeans, also regarded as phytoestrogen because of its structural resemblance with female estrogen hormone and its estrogenic activity **[**Fig. 1**(a)]**. It exhibits myriads of biological activities including potential cardioprotective effects, lowers the risk of prostate cancer and colon cancer, neuroprotective effect against Alzheimer's disease, reduces the negative impact of menopause on females and effective in treatment of non-alcoholic fatty liver disease (NAFLD) [2,3].

Despite, its tremendous biological activities, it exhibits poor aqueous solubility (which drastically reduces its bioavailability) and rapid *in-vivo* metabolism (glucuronidation and sulfation), which hampers its use in functional foods and food supplements [4–6].To overcome these limitations cyclodextrin (CD) complexes are gaining tremendous attention in recent years to enhance the aqueous solubility, stability and bioavailability of phytochemicals [7].

CDs are macrocyclic oligosaccharides consisting of α-(1,4)-linked glucopyranose units, that are originated from glucosyltransferase-mediated enzymatic hydrolysis of starch [8,9]. There are three natural CDs derived on the basis of number of glucopyranose units, namely α-CD (6 units), β-CD (7 units), and γ-CDs (8 units) [10]. Among all, β-CDs are more affable due to their appropriate cavity size and economic cost as compared to α-CD and γ-CDs [11,12]. In recent years, more focus has been

* Corresponding authors at: Biotechnology Division CSIR – Institute of Himalayan Bioresource Technology, Palampur 176061, Himachal Pradesh, India (R. Purohit) and Dietetics and Nutrition Technology Division, CSIR – Institute of Himalayan Bioresource Technology, Palampur 176061, Himachal Pradesh, India (A. Saneja).
E-mail addresses: rituraj@ihbt.res.in, riturajpurohit@gmail.com (R. Purohit), ankitsaneja@ihbt.res.in, ankitsaneja.ihbt@gmail.com (A. Saneja).

https://doi.org/10.1016/j.molliq.2023.121295
0167-7322/

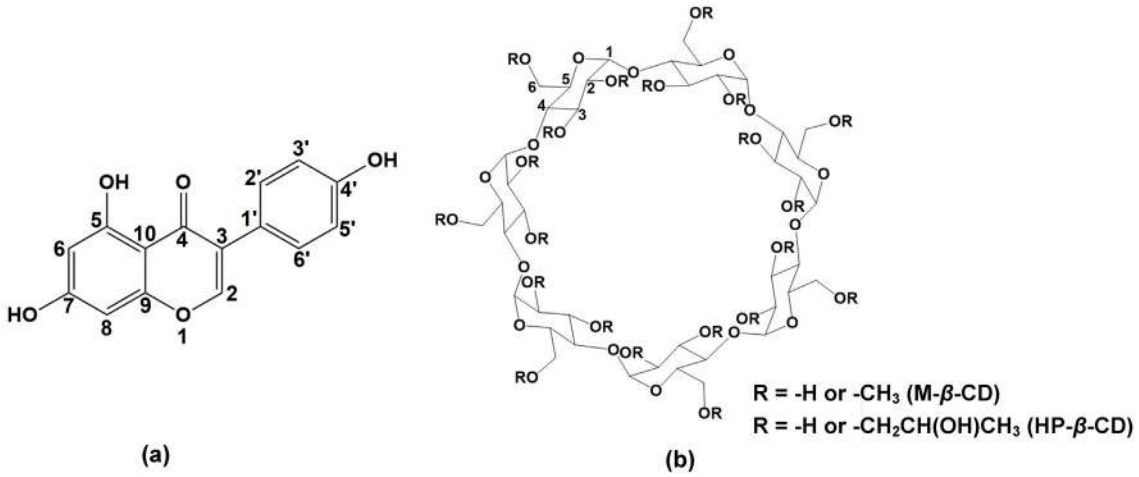

Fig. 1. Schematic representation of chemical structures of (a) genistein (b) β-cyclodextrin, where R represents the substitution of –H or $–CH_3$ in case of methyl-β-cyclodextrin (M-β-CD) and substitution of –H or $–CH_2CH(OH)CH_3$ in case of hydroxypropyl-β-cyclodextrin (HP-β-CD).

given towards modified forms of β-CDs, such as hydroxypropyl-beta-CD (HP-β-CD) and methyl-beta-CD (M-β-CDs) **[**Fig. 1**(b)]** [13]. These forms are modified to overcome the toxicity, undesirable properties, solubility issues, stability issues (provide protection against oxidation and light-induced reactions) and pose better inclusion ability than the natural CDs [14–19]. Moreover, various studies conducted in past demonstrated that these modified forms of β-CDs could effectively form inclusion complexes with isoflavones [5,20].

In the last decade, various studies have been carried out to find out molecular interaction and binding affinity of phyto-active molecules with CDs through different techniques such as circular dichroism, Raman scattering, neutron scattering, UV & FT-IR spectroscopy and molecular dynamics (MD) simulations [21–26].

However, in the present investigation, the experimental approach was correlated for the first time with microsecond time-scale explicit-solvent molecular dynamics simulations to illustrate the dynamics of inclusion complex formation between GEN and modified β-CDs**.** In addition, we also explored the conformational space of ICs by enhanced sampling simulations, which reflect equilibrium conditions in more efficient manner as compared to conventional MD simulations, thereby allowing accurate fabrication of free energy landscapes [27,28].

In this regard, the phase solubility studies were conducted to determine the molar stoichiometric ratio and the encapsulation capability of β-CD and its derivatives (M-β-CD and HP-β-CD). The ICs of GEN were prepared with modified forms of β-CD (M-β-CD and HP-β-CD) through the spray-drying technique. The ICs were characterized by FT-IR, Powder-XRD, SEM and NMR spectroscopy (^{1}H NMR & 2D – NOESY). As the experimental methods for preparation and characterization are somehow limited to clearly demonstrate the key structural features and the dynamics involved in the formation of CD ICs. Hence, we further employed classical MD simulations and enhanced umbrella sampling simulations on two modified β-CD derivatives to get molecular-level insights into CD complex formations.

2. Materials and methods

2.1. Materials

Genistein ($C_{15}H_{10}O_5$, MW: 270.24 g/mol, >98 % Purity, Cas No. 446–72-0), β-cyclodextrin (MW: 1134.99 g/mol, >99.0 % Purity, Cas No. 7585–39-9), methyl-β-cyclodextrin (mixture of several methylated, Cas No. 128446–36-6), hydroxypropyl-β-cyclodextrin (Cas No. 128446–35-5) were purchased by Tokyo Chemical Industry Co., ltd. Deuterium oxide (“100 %”, ≥99.96 atom %D, Cas No. 7789–20-0), DMSO d_6 (“100 %”, ≥99.96 atom %D, contains 0.03 % (v/v) TMS, Cas No. 2206–27-1) were purchased from Sigma Aldrich. All other chemicals and reagents used were of analytical grade unless otherwise stated.

2.2. Matrix-assisted laser desorption ionization/ time-of-flight (MALDI-TOF) mass spectrometry

The mass spectrum of M-β-CD and HP-β-CD was obtained by a MALDI-TOF-TOF mass spectrometer (Bruker, Ultraflex TOF/TOF, USA). During analysis, 0.5 μL of the CDs (M-β-CD & HP-β-CD) solution was placed on a metal plate and mixed with 0.5 μL of matrix solution (α-cyano-4-hydroxycinnamic acid). The MALDI-TOF spectra were recorded from mass range 700 to 2000 Da in positive ion reflector mode. Approximately, 3000 laser shots (for M-β-CD) and 5500 laser shorts (for HP-β-CD) in were averaged to obtain the representative mass. Data were analyzed using FlexAnalysis software (Bruker Daltonics) [29].

2.3. Phase solubility studies

Phase solubility studies were conducted accordingly as reported earlier with minor modifications [30]. A surplus amount of GEN was added in eppendorf tubes with 2 mL of β-CD, M-β-CD and HP-β-CD aqueous solution at various concentrations (0 to 10 mM), separately. The tubes were incubated in IKA® matrix orbital shaker (Delta F2.0, Germany) at 37 °C with constant shaking for 48 h in dark and obtained suspension was filtered through 0.22 μm membrane filter. The extent of the solubility of GEN was measured through HPLC (Waters 2000) equipped with empower software utilized for data acquisition and analyzed on a pheominix 100–5 C18 column (250 × 4.6 mm, 5 μM) with isocratic elution (60:40 *v/v*) (Eluent A: Methanol; Eluent B: 0.1 % Trifluoroacetic acid in water) with signal determination by PDA UV detector at 261 nm by the method reported by Tabar et al. with minor modifications [31]. The phase solubility curves were plotted between the molar concentration of CDs and the molar concentration of GEN and the stability constant (Ks) was calculated from the slope of the plot as per Higuchi-Connor’s equation:

$$K_S = \left[\frac{Slope}{S_0(1 - Slope)}\right] \quad (1)$$

Where S_0 is the concentration of GEN in absence of CDs and slope can be expressed from linear equation of phase solubility curves. The experiments are conducted in triplicates and results were expressed as mean ± SD (n = 3).

2.4. Preparation of GEN: CD inclusion complexes (ICs)

The CDs that demonstrated the maximum solubility and apparent stability constant from phase solubility studies were chosen to prepare GEN ICs in a 1:1 M stoichiometric ratio (GEN:CD). Briefly, GEN (5 mM, 0.27 g) solution was prepared in ethanol (40 mL) and M-β-CD (5 mM, 1.30 g) was dissolved in 160 mL of Milli-Q water. Similarly, the GEN-HP-β-CD ICs was prepared by dissolving HP-β-CD (5 mM, 1.53 g) in MQ water, both the solution were mixed (GEN and CD solution) and placed over a magnetic stirrer for 24 h. The obtained solution was fed for spray-drying in Buchi Mini Spray Dryer (B-290, Switzerland) with specified conditions of inlet temperature at 120 °C ± 5 °C and outlet temperature of 75 ± 5 °C, respectively; feed rate of 4 mL/min; aspiration rate of ~ 80 % [32–35]. Spray-dried GEN/CD powders were collected from the cyclone and stored in a tightly sealed container and kept in the refrigerator till further use.

2.5. Preparation of the physical mixtures

The physical mixture was prepared for comparative study by the simple blending of GEN:CD (1:1) for 15–20 min in a ceramic mortar pestle and obtained pulverized powders were sieved, stored in bottles and kept in the refrigerator [15].

2.6. Characterization of inclusion complexes (ICs)

2.6.1. Fourier-transform infrared spectroscopy (FT-IR)

The FT-IR spectra of GEN, M-β-CD, HP-β-CD, their respective physical mixtures and inclusion complexes were recorded in the range of 4000 cm^{-1} to 500 cm^{-1}. Prior to analysis, samples were compressed with KBr by hydraulic press to form KBr disks. The spectra were recorded using FT-IR spectrophotometer (PerkinElmer, equipped with software Spectrum ES version 10.5.3, USA) [36].

2.6.2. Powder X-ray diffractometry (PXRD)

PXRD patterns were recorded on smartLab 9 kW rotating anode X-ray diffractometer (Rigaku Corporation, Tokyo, Japan) equipped with a Cu-Kα radiation source. Before exposure of samples to the X-ray beam, they were tightly packed in a rectangular aluminum cell. The data were collected at diffraction angle 2θ from range of 5°- 60° with a scan rate of 10°/min and step size of 0.02° [15].

2.6.3. Scanning electron microscopy (SEM)

Morphological evaluation of GEN, M-β-CD, HP-β-CD, their respective physical mixtures and inclusion complexes was performed by SEM (S-3400 N SEM, Hitachi, Tokyo, Japan). For analysis, a small stretch of double-sided carbon tape was fixed on a metal stub and the samples were spreaded over the adhesive tape. Before the analysis, the samples were coated with gold–palladium under an argon atmosphere by utilizing an Ion sputter coater (Hitachi E-1030) to make them electrically conductive.

2.6.4. Nuclear magnetic resonance (NMR)

^{1}H NMR spectra of GEN, M-β-CD, HP-β-CD, GEN/M-β-CD and GEN/HP-β-CD ICs and 2D-NOESY spectra of CD-ICs were recorded to investigate the average extent of penetration and stereochemical interactions between host and guest molecule. The NMR spectra were recorded at room temperature on NMR spectrometer (AV-600, Bruker) using D_2O/DMSO d_6 (600 μL) as a solvent. The chemical shifts were expressed in parts per million (ppm) [37].

2.6.5. Computational datasets and modeling of inclusion complexes (ICs)

The structures of GEN (CAS Number: 446–72-0), HP-β-CD (CAS Number: 128446–35-5) and M-β-CD (CAS Number: 128446–36-6), were downloaded in sdf format from the Pubchem database [38]. The 2D structure files were converted to 3D format and subjected to geometry and energy minimization by the steepest descent method (1000 steps) of Discovery Studio package [39]. The CDOCKER protocol of Discovery Studio was utilized for modeling the GEN/HP-β-CD and GEN/M-β-CD ICs. CDOCKER produced 10 conformations each for both the complexes. The models with least interaction energy scores were selected for further investigations.

2.7. Molecular dynamics (MD) simulations

The modeled GEN/HP-β-CD and GEN/M-β-CD ICs were selected as starting structures for MD simulation studies by GROMACS software [40–42]. The MD simulations for both the complexes were carried out in different steps including topology generation, solvation, energy minimization, equilibration and finally subjected to MD production runs of 1000 ns (1 μs) each. The structural coordinates of GEN, HP-β-CD, and M-β-CD were extracted from the complex files and submitted to the PRODRG server for the generation of topologies compatible with GROMOS force fields [43]. The GEN topologies were amended to HP-β-CD, and M-β-CD topologies and the resulting structures were placed inside a cubic simulation box filled with a simple point charge water model. The number of water molecules added in simulation box having GEN in complex with HP-β-CD, and M-β-CD were 2875 and 2151 respectively. In the next step, steric clashes or inappropriate geometry were removed by structure relaxation through energy minimization. The steepest descent minimization protocol with a maximum of 50,000 steps and a maximum force cut-off value of < 1000.0 kJ/mol/nm was used for energy minimization. The equilibration of the system was achieved in two steps under: 1000 ps NVT (particle number, volume, and temperature are kept constant) and 1000 ps NPT (particle number, pressure, and temperature are all constant) ensembles. The temperature of the system was maintained at 300 K by V-rescale (modified Berendsen thermostat), while 1 bar reference pressure was maintained by the Parrinello-Rahman algorithm [44,45]. The leap-frog integrator with a 2 fs time step was used for the integration of the equations of motion. The SHAKE algorithm was employed for constraining bond lengths involving hydrogen atoms, while the long-range interactions were included by the Particle-Mesh Ewald (PME) method [46,47]. The energy minimized and well-equilibrated structures were then allowed for production MD runs of 1000 ns. The built-in scripts of GROMACS software were used for the analysis of the resulting MD trajectories of both the complexes.

2.8. Calculation of Gibbs free energy potential

The eigenvalues and related eigenvectors were produced by diagonalizing the covariance matrix, which was created using the atomic Cartesian space. The matrix's element (Cij) can be defined as follows:

$$C_{ij} = \langle (X_i - \langle X_i \rangle)(X_j - \langle Xj \rangle) \rangle (i, j = 1, 2, 3, \cdots\cdots\cdots..N) \quad (2)$$

where N is the number of chosen atoms, <Xi > is the average atomic location, and Xi is the ith atom's Cartesian coordinates. As a result, the direction is represented by the eigenvector of the matrix, and

the magnitude of motion in that direction is represented by the eigenvalue.

As reaction coordinates, the PC1 and PC2 components of the MD trajectories were used. The FEP was generated using PCA data. the FEP was calculated as follows:

$$G(PC1, PC2) = -KBT \ln P(PC1, PC2) \quad (3)$$

where P (PC1, PC2) represents the system's probability distribution along coordinate PC, G denotes Gibbs free energy, KB signifies the Boltzmann constant, T is the simulated temperature, and all other variables are constants. In this study, the free energy was employed as the third coordinate to construct the FEP by projecting the energy landscape into the 3-dimensional space defined by the first two principal components (PC1 and PC2).

2.9. Umbrella sampling simulations

Umbrella sampling is a computational technique that improves the sampling of a system where ergodicity is obstructed by the form of the system's energy landscape [48]. The structures corresponding to the least energy obtained from the analysis of Gibbs free energy landscape were subjected to umbrella sampling simulations. The umbrella sampling simulations were also carried out by the GROMACS package. First of all, a series of configurations along a reaction coordinate were generated by forcing the ligand molecule (GEN) to move out of the binding site along the unbinding pathway. A constant force of 250 kJ/mol/nm^2 was applied at a pull rate of 0.01 nm/ps through a virtual spring to simulate the unbinding of the ligand molecule. The configurations so obtained were scrutinized based on center of mass (CoM) distance for umbrella sampling windows, which were run in independent simulations. For the initial 3 nm CoM distance, the sampling windows were collected after every 0.15 nm, while a window spacing of 2.0 nm was selected for CoM distance>3 nm. The dynamic sampling of spacing windows allowed enhanced details at lower CoM distances. A total of 80 sampling windows for both the complexes were generated and each configuration was independently subjected to 10 ns umbrella sampling simulations, resulting in a total of 800 ns simulation time. Finally, the Weighted Histogram Analysis Method (WHAM) was utilized to extract the potential of mean force (PMF) curves [49]. The bootstrap method was used for error estimation and the binding energy (ΔG_{bind}) was calculated from the PMF curves of the complexes.

3. Results and discussions

3.1. Mass spectrum of M-β-CD and HP-β-CD

The MALDI-TOF mass spectrum of M-β-CD demonstrated specific peaks corresponding to its average molecular weight of (Mw) ~ 1301.7 which is similar to results obtained from previous study [50]. Additionally, a peak difference of 15 Da was observed between each peak of M-β-CD which corresponds to the one methyl substitution **[Supplementary Figure S1 (a)].** Similarly, HP-β-CD demonstrated average molecular weight of Mw ~ 1539. **[Supplementary Figure S1 (b)]** [29]. The variation in the peak is associated with the degree of substitution of hydroxypropyl moiety (MW: 58 g/mol) on HP-β-CD. As the molecular weight of β-CD is 1135 g/mol, it can be concluded that approximately 8–16 methyl groups and 2–12 hydroxypropyl moieties were linked to each M-β-CD and HP-β-CD molecule, respectively **[Supplementary Table S1].**

3.2. Phase solubility studies

As a preliminary screening step, the phase solubility studies were conducted to determine the molar stoichiometric ratio, stability constants (Ks) and solubilizing capability of different CDs towards GEN. The phase solubility curves of GEN with β-CD, M-β-CD and HP-β-CD are represented in **[**Fig. 2**].** The phase solubility curve represents a linear increment ($R^2 \geq 0.99$) in the aqueous solubility of GEN with CDs in concentration dependent manner (0–10 mM) **[Supplementary Figure S4].** Moreover, all phase solubility curves indicated A_L-type curve which represents that the guest molecule (GEN) and host molecule (CDs) interacted to form ICs with a molar/stoichiometric ratio of 1:1 as per Higuchi and Connors [16,51].

It was also observed that aqueous media with 10 mM of their respective CDs concentration cause remarkable enhancement in solubility of GEN/M-β-CD (~164 folds) and GEN/HP-β-CD (~104 folds) in the complex as compared to free GEN (without CDs). These outcomes display that both M-β-CD and HP-β-CD have high potential to enhance GEN solubility and hence, are the ideal carriers for GEN.

The apparent stability constant (K_s, M^{-1}) of GEN/CDs ICs were determined from the slopes of linear phase solubility curves and ranked in the order: M-β-CD (20005.98, very strong binding) > HP-β-CD (11587.10, strong binding) > β-CD (3662.58, moderate binding) which is approximately in the range as per earlier reports [16,52] **[Supplementary Table S2].** As per Jacob et al., the greater the apparent stability constant (Ks, M^{-1}) value, the stronger will be the binding affinity between host and guest molecule. Moreover, Ks value ranging from 1000 – 5000 M^{-1} represents a moderate binding, while value ranging from 5000 – 20,000 M^{-1} indicates strong binding and ks > 20,000 M^{-1} represents very strong binding [53]. In the present study, M-β-CD exhibited the strongest binding affinity towards GEN, followed by HP-β-CD and β-CD. Although all three CDs consist of seven glucopyranose units (similar molecular cavities), despites, a significantly higher stability constant was found in the case of modified β-CDs to form ICs with GEN than the native β-CD. This may be attributed to extension in the hydrophobic domain at inner cavity therefore improving the binding potential of genistein which eventually results in enhanced solubility of genistein [54,55].

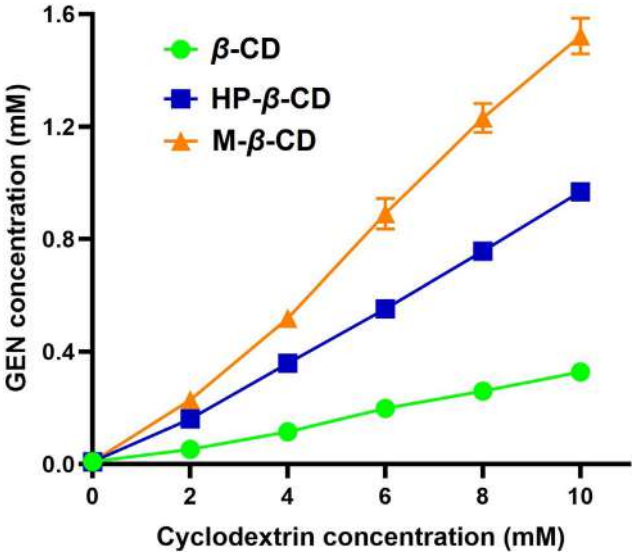

Fig. 2. Phase solubility curve of genistein in aqueous solutions of β-cyclodextrin (green), M-β-CD (orange) and HP-β-CD (blue) with different concentrations (0–10 mM). The values were expressed as mean ± standard deviation (n = 3).

3.3. Characterization of inclusion complexes (ICs)

3.3.1. Fourier-transform infrared spectroscopy (FT-IR) analysis

The FT-IR spectra of GEN, M-β-CD, HP-β-CD, ICs and their physical mixtures are shown in **[**Fig. 3 **(a)]**. The spectrum of GEN displayed several intense and sharp absorption bands with its characteristic peaks at 3410 cm^{-1} and 3088 cm^{-1}, representing stretching vibrations of –OH and aromatic –CH groups, respectively. Additionally, the peaks at 1652 cm^{-1} and 1615 cm^{-1} reflect vibrational C=O stretching frequency and C=C stretching, absorption bands from 1320 to 1150 cm^{-1} represents C—O—C stretching, while absorption bands ranging from 1260 to 1000 cm^{-1} corresponds to C—O stretching [21,56]. The spectrum of M-β-CD demonstrated a prominent absorption band of O—H stretching vibration at 3415.32 cm^{-1}, C—H stretching vibration peak at 2936.75 cm^{-1} and peaks due to C—H and C—O stretching vibrations at 1159.79, 1085.00 and 1044.39 cm^{-1}, which is similar to the observations reported in previous studies [37,57]. The FT-IR spectrum of HP-β-CD demonstrated a characteristic absorption band at 3409.41 cm^{-1} due to the hydrogen-bonded hydroxyl groups undergoing symmetrical and asymmetrical stretching vibration. Further, a peak at 2929.99 cm^{-1} is assigned for stretching vibration of the C—H bond and some other prominent bands at 1638.80 cm^{-1}, 1157.90 cm^{-1}, 1033.60 cm^{-1} denoted H—O—H bending, C—O stretching vibration, and C—O—C vibration, respectively [36,58,59]. The FT-IR spectra of respective physical mixtures showed characteristics peak of GEN and CDs with stacking effect, indicates simple overlapping of GEN and CDs spectra with weak or no interaction between GEN and CDs [16,37]. Additionally, in spectra of physical mixtures, the characteristic peak of GEN at 3410.30 cm^{-1} demonstrated reduced intensity, whereas it was completely masked by the very intense and broad CDs bands in the ICs, which may be possibly due to the participation of OH groups of GEN with the host (CDs) *via* the H-bonding [34]. Moreover, some of the characteristics absorption bands of GEN demonstrated reduced intensity (1500 cm^{-1} –1000 cm^{-1}) or get completely concealed (peak of GEN at 3410.30 cm^{-1} and region from 3000 cm^{-1} –2000 cm^{-1}) by the CDs (highlighted with different colors in Fig. 3(a) with no appearance of new absorption band after the formation of IC). Similar observations are reported in literature, where the characteristic absorption peaks of the guest molecule were shifted, decreased or masked as an indicative of the incorporation of the guest molecule inside the host cavity [34,60–62]. The noticeable differences in the FTIR spectrum of free GEN and the complex state give a fair impression of the possible molecular interactions between GEN and CD cavities. However, further experiments were performed to confirm the formation of ICs.

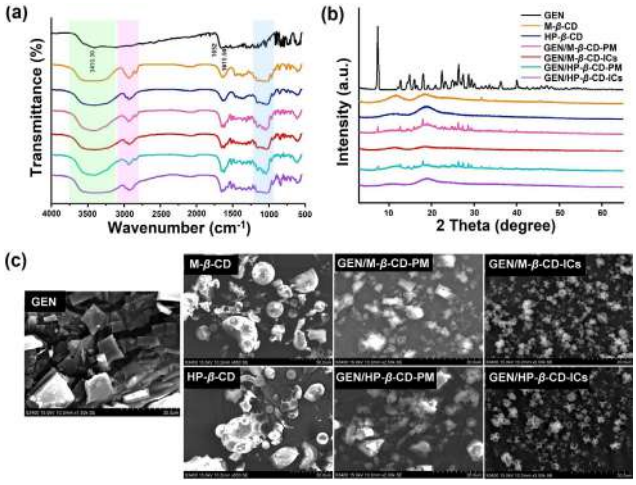

Fig. 3. Solid state characterization of developed inclusion complexes (ICs) using (a) FTIR, (b) PXRD spectra and (c) SEM. The FTIR spectra, green, pink and blue regions indicate shifted, decreased and concealed characteristic absorption peaks of genistein after inclusion complex formation.

3.3.2. Powder X-ray diffractometry (PXRD) analysis

PXRD is an effective analytical technique for the characterization of inclusion complexes. The PXRD patterns of GEN exhibit several sharp peaks at diffraction angles such as 7.38°, 14.82°, 18.04°, 22.44°, 26.38°, 27.40°, 28.68° revealed its crystalline structure as reported earlier [63] **[**Fig. 3**(b)]**. M-β-CD and HP-β-CD exhibited smooth curves without crystalline peaks due to their natural amorphous state as reported [15,36,64]. The XRD diffractogram of physical mixtures of GEN with M-β-CD and HP-β-CD represented combined characteristic patterns of GEN with their respective CDs, with significantly weakened characteristic peaks of GEN as compared to the diffractogram of pure GEN. In contrast, the PXRD spectra of GEN-CD ICs demonstrated an amorphous pattern that was similar to the diffractogram of their parent CD with complete concealing of the crystallization peaks of GEN. It may be concluded that in the process of formation of ICs, the GEN molecule encapsulated inside CD cavities and thereby preventing the aggregation of GEN molecules to form crystals. This observation served as conclusive evidence of the formation of inclusion complexes and transition of GEN from crystalline to amorphous form.

3.3.3. Scanning electron microscopy (SEM) studies

Comparative analysis of intuitive images obtained from the SEM experiment provides morphological evidence of the successful formation of ICs **[**Fig. 3 **(c)]**. The SEM micrograph of GEN displayed its well-defined crystal structure [5]. The surface morphology of M-β-CD and HP-β-CD revealed porous and spherical shape structures with cavity size variability and cavity fragments, indicating its amorphous nature [29,36,51,64]. However, the SEM images of the physical mixtures displayed a mixture of distorted spherical particles with crystals of GEN adhered over the surface of CDs. Comparatively, the surface morphology of spray-dried obtained CD complexes of GEN reveals amorphous and homogenous sphere-shaped structures with some uneven surfaces [65,66]. This significant change in surface morphology of inclusion complexes represented the presence of a new solid phase, effective encapsulation of GEN and efficiency of the spray drying mechanism.

3.3.4. Nuclear magnetic resonance (NMR) analysis

The intermolecular interactions between guest–host assembly can be elucidated using nuclear magnetic resonance (NMR) spectroscopy by analyzing the chemical shift difference in the NMR spectrum before and after the inclusion complex formation [55,67]. Thus, we performed ^{1}H NMR to reveal the formation of the ICs by comparing the chemical shift changes among GEN, CDs and GEN-CD – ICs **[**Fig. 4 **(a)]**.

The ^{1}H NMR spectra of GEN depict peaks at ~ 12.97 ppm, ~10.86 ppm and ~ 9.58 ppm due to –OH groups of H-5-OH (s), H-7-OH (s), and H-4′-OH (s), respectively. Additionally, peaks at ~ 8.30 ppm, ~7.37 ppm, ~6.83 ppm, ~6.37 ppm and ~ 6.22 pp m were observed due to H-2 (s), H-2′,6′ (d), H-3′,5′ (d), H-8 (s) and H-6 (s) respectively [68,69]. The chemical shifts of HP-β-CD were observed at δ values ~ 4.83 ppm, ~3.47 ppm, ~3.75 ppm, ~3.40 ppm, ~3.56 ppm, ~3.61 ppm and ~ 1.02 ppm due to H-1, H-2, H-3, H-4, H-5, H-6 and protons of the methyl group, respectively [36,70–72]. The M-β-CD showed characteristics chemical shifts δ values at ~ 4.91 ppm, ~3.60 ppm, ~3.77 ppm, ~3.51 ppm, ~3.50 ppm, ~3.71 ppm due to H-1, H-2, H-3, H-4, H-

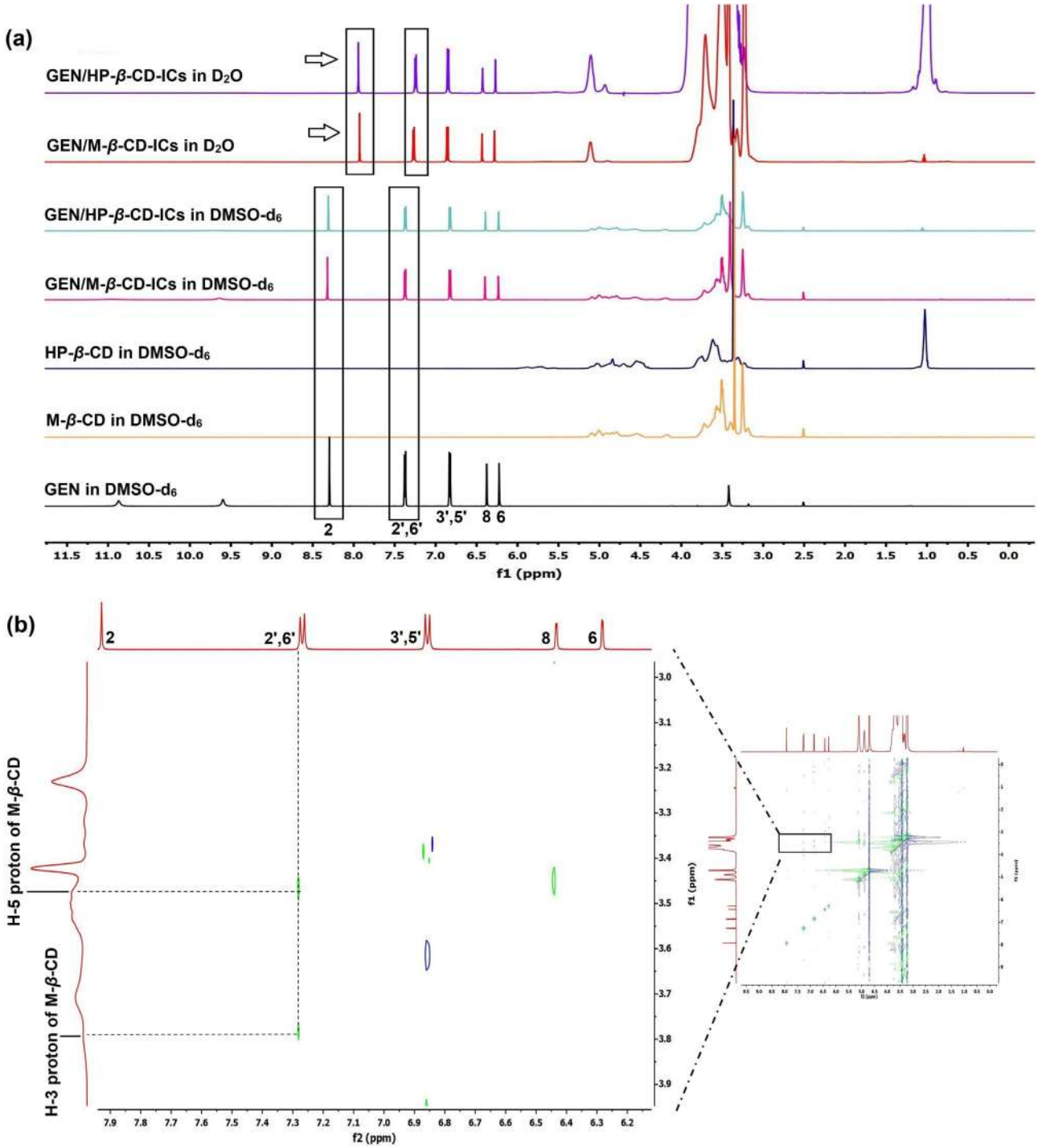

Fig. 4. Nuclear magnetic resonance spectroscopy characterization of inclusion complexes (ICs) (a) ^{1}H NMR of GEN, M-β-CD, HP-β-CD and their ICs in DMSO d_6 & D_2O and (b) 2D-NOESY spectra of GEN/M-β-CD-ICs and (c) GEN/HP-β-CD-ICs in D_2O. The chemical shift at 4.79 ppm and 2.50 ppm was observed due to D_2O & DMSO d_6.

5 and H-6 protons and ~ 3.25 ppm due to methyl group protons, respectively [57,73,74] **[Supplementary Table S3]**.

In order to confirm the inclusion of GEN inside CD cavities, a comparison of GEN proton spectra in the free state and complexed state was performed. The proton NMR spectrum of the ICs in D_2O represented the direct evidence of the inclusion of GEN inside the cavities of CDs as all expected aromatic protons of GEN were clearly observed in spectra (although GEN possess very low aqueous solubility) which is in correlation with previous reports [37,75]. Moreover, protons of GEN in ICs (in D_2O) exhibited significant downfield and upfield shifts **[**Fig. 4**(a)]**. It can be clearly observed in GEN-M-β-CD-ICs spectra that H-2, H-2′ and H-6′ proton of GEN demonstrated significant upfield shifting ($\Delta\delta$) of −0.370 ppm, −0.100 ppm and −0.100 ppm, respectively [calculated from equation ($\Delta\delta = \delta_{complex} - \delta_{free\ GEN}$)] **[**Fig. 4**(a)]**. Whereas, H-6, H-8, H-3′ & H-5′ displayed slight downfield shift ($\Delta\delta$) of 0.060, 0.060, 0.030 and 0.030 respectively, similar shifting has been observed in the case of GEN/HP-β-CD ICs **[Supplementary Table S3].**

We also utilized 2D - NMR technique to get a deep insight into the modes of inclusion of guests inside the host cavities [76]. The

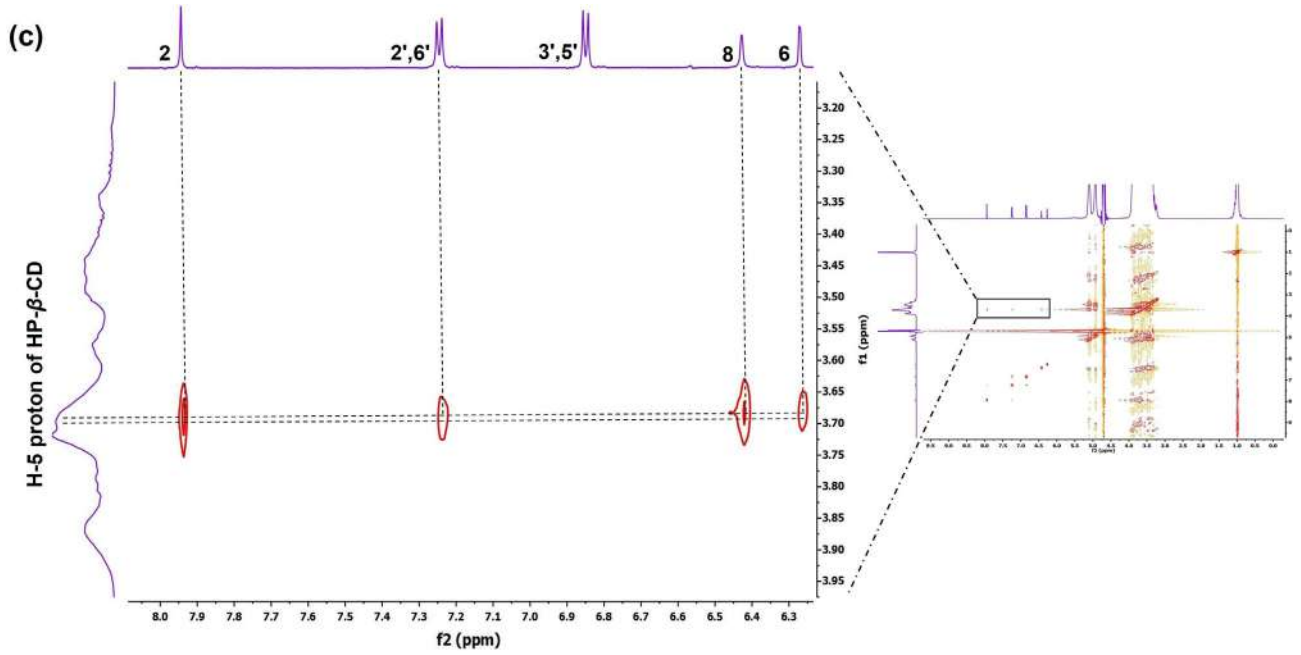

Fig. 4 (*continued*)

nuclear overhauser effect (NOE) is a common phenomenon that occurs between the atoms in close proximity to each other, due to the transfer of the spin polarization from one group of nuclear spins to another [77,78]. NOE-based experiments provide spatial proximity between host–guest assembly by observation of all intermolecular cross-peak correlations in the spectrum, making data interpretation easier and simple. The most common NOE-based 2D NMR techniques applied for structural elucidation of ICs are 2D-NOESY (Nuclear Overhauser Effect Spectroscopy) [76,78,79]. Thus, to decipher the molecular interactions of the ICs, we further carried out 2D-NOESY analysis.

Usually, it was observed that after the formation of ICs, there is an increase in electron density over the CD protons inside the cavity (H-3 and H-5) which leads to alteration in chemical shifts while the protons lying exterior to the cavity (H-1, H-2 and H-4) remain unaffected [80]. The 2D-NOESY spectra of GEN/ M-β-CD ICs displayed that there was a key correlation between the aromatic doublets (7.27 ppm, H-2′,6′) of the 4-hydroxyphenyl moiety of GEN with H-3 and H-5 protons of M-β-CD and also cause induced shifting of protons present in the inner cavity of M-β-CD, [H-3 ($\Delta\delta$: 0.030 ppm) and H-5 protons of ($\Delta\delta$: −0.026 ppm)] **[**Fig. 4 **(b)]**. In contrast, the 2-D NOESY spectrum of GEN/ HP-β-CD ICs demonstrated cross-correlation peaks between H-2, H-2′,6′, H-8 and H-6 protons of GEN with the H-5 protons of HP-β-CD. Consequently, causing induced downfield shifting of H-5 protons of HP-β-CD ($\Delta\delta$: 0.131) **[**Fig. 4 **(c)]**. The above correlation reveals that the phenyl ring of GEN is inserted inside the M-β-CD from the wider side of the rim. While in the case of HP-β-CD, the chromone ring of GEN is entered inside the HP-β-CD cavities from the wider rim edge. In the present study, the GEN inclusion complex demonstrated similar mode of orientations as reported in recent studies with natural bioactive molecules such as phloretin [16,51], naringenin [81,82], myricetin [75], daidzein [17,83,84], apigenin [85,86], fisetin [87], and baicalein [88] where two considerably different binding modes were observed. The two different orientation modes of GEN inside the methyl and hydroxypropyl substituted CDs may be due to the arrangement of these substitution group during the inclusion formation and their flexibility to alter the CD conformation.

3.4. Conformational stability of selected ICs

The conformational stability of the modeled GEN/HP-β-CD and GEN/M-β-CD ICs was accessed by calculating the RMSD for the whole simulation run **[**Fig. 5**(a)]**. The stability of a complex is inversely related to the number of deviations occuring during the simulations. We observed no major deviations in the RMSD values for both the complexes. Although the overall trajectory was stable, minor deviations at two different time intervals (∼300–500 ns and ∼ 700–750 ns) were observed for GEN/M-β-CD complex. These deviations suggested multiple stable conformations achieved by GEN/M-β-CD complex during the simulations. The average RMSD values for GEN/HP-β-CD and GEN/M-β-CD ICs were 0.416 nm and 0.417 nm respectively. The low deviations and stable trajectories for both the complexes suggested high equilibration and conformational stability during the simulations.

3.5. Compactness of ICs

In order to compare the encapsulation process of GEN into HP-β-CD and M-β-CD during MD simulations, the compactness and packaging of both the ICs were determined by accessing their Radius of gyration (Rg) **[**Fig. 5**(b)]**. Rg illustrates the mass-weighted root mean square distance from the center of mass of atoms under investigation [89]. Several computational studies have utilized Rg for the estimation of the compactness of protein [90], protein–ligand [91,92], and CD-IC structures [93]. The Rg curves showed that GEN/M-β-CD had lower Rg values than GEN/HP-β-CD throughout the simulations. Moreover, the difference in Rg values was calculated as Rg_dif (Rg_IC-(Rg_guest + Rg_host)) and compared for GEN/HP-β-CD and GEN/M-β-CD structures **(**Table 1**)**. We observed a lower value of Rg_dif for GEN/M-β-CD (-0.407 ± 0.010) than GEN/HP-β-CD (-0.396 ± 0.017). Lower average Rg and Rg_dif values indicated higher compactness and tighter packaging of GEN/M-β-CD than GEN/HP-β-CD. These results also resonate with experimental solubility studies, where GEN was shown to be more soluble in M-β-CD than HP-β-CD.

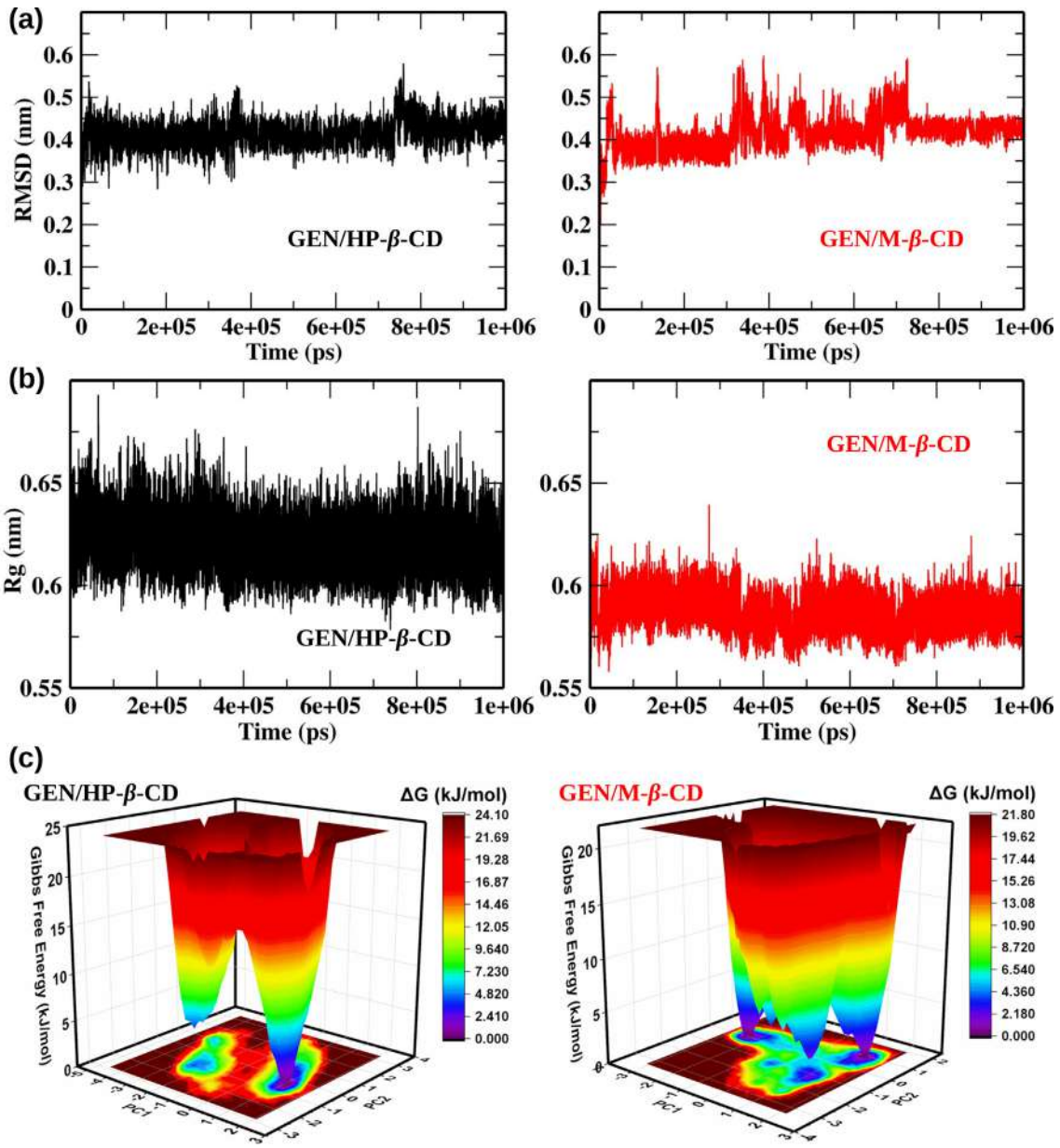

Fig. 5. Assessing stability of modelled GEN/β-CD derivatives inclusion complexes (ICs) by classical MD simulations. (a) Root mean square deviations (RMSD) of backbone Cα atoms of GEN/HP-β-CD and GEN/M-β-CD ICs (b) Radius of gyration for GEN/HP-β-CD and GEN/M-β-CD ICs, and (c) Gibbs free energy potential (FEP) showing local minimas for GEN/HP-β-CD and GEN/M-β-CD ICs.

Table 1
Comparison of Rg values for GEN/HP-β-CD and GEN/M-β-CD structures.

Inclusion complex	Rg_host (nm)	Rg_guest (nm)	Rg_IC (nm)	Rg_dif = (Rg_IC-(Rg_guest + Rg_host))
GEN/HP-β-CD	0.636 ± 0.012	0.379 ± 0.003	0.619 ± 0.011	−0.396 ± 0.017
GEN/M-β-CD	0.614 ± 0.007	0.379 ± 0.003	0.586 ± 0.007	−0.407 ± 0.010

3.6. Gibbs free energy potential (FEP)

The FEP reflects the kinetics and thermodynamics of any molecular processes in solution. The FEP graphs are generally analyzed for the detection of the most stable conformations achieved by a given system during MD simulations. The graphs for Gibbs FEPs were plotted for GEN/HP-β-CD and GEN/M-β-CD ICs from the MD trajectories by Boltzmann inverting multi-dimensional histograms method **[**Fig. 5 **(c)]**. In order to explore the conformational shifts during the binding process of GEN with substituted β-CDs, the Gibbs FEP for the first two principal components (PC1 and PC2) was calculated. The first two PCs are usually the most vital among all the PCs to analyze the changes in Cα displacements during MD simulations. The metastable conformation achieved by structures are shown by the deep low free energy valleys, while the shallow basins depict energetic barriers connecting these states. The

GEN/HP-β-CD IC showed a single deep valley achieving the least value of free energy. In the case of modeled GEN/M-β-CD structure, we observed two distinct energy minimas which correspond to metastable conformations. These results are consistent with the RMSD analysis, where GEN/HP-β-CD showed deviations at two distinct time intervals. Further, we investigated different binding poses opted by GEN and both the modified β-CDs by extracting the trajectories of both the complexes at different time intervals.

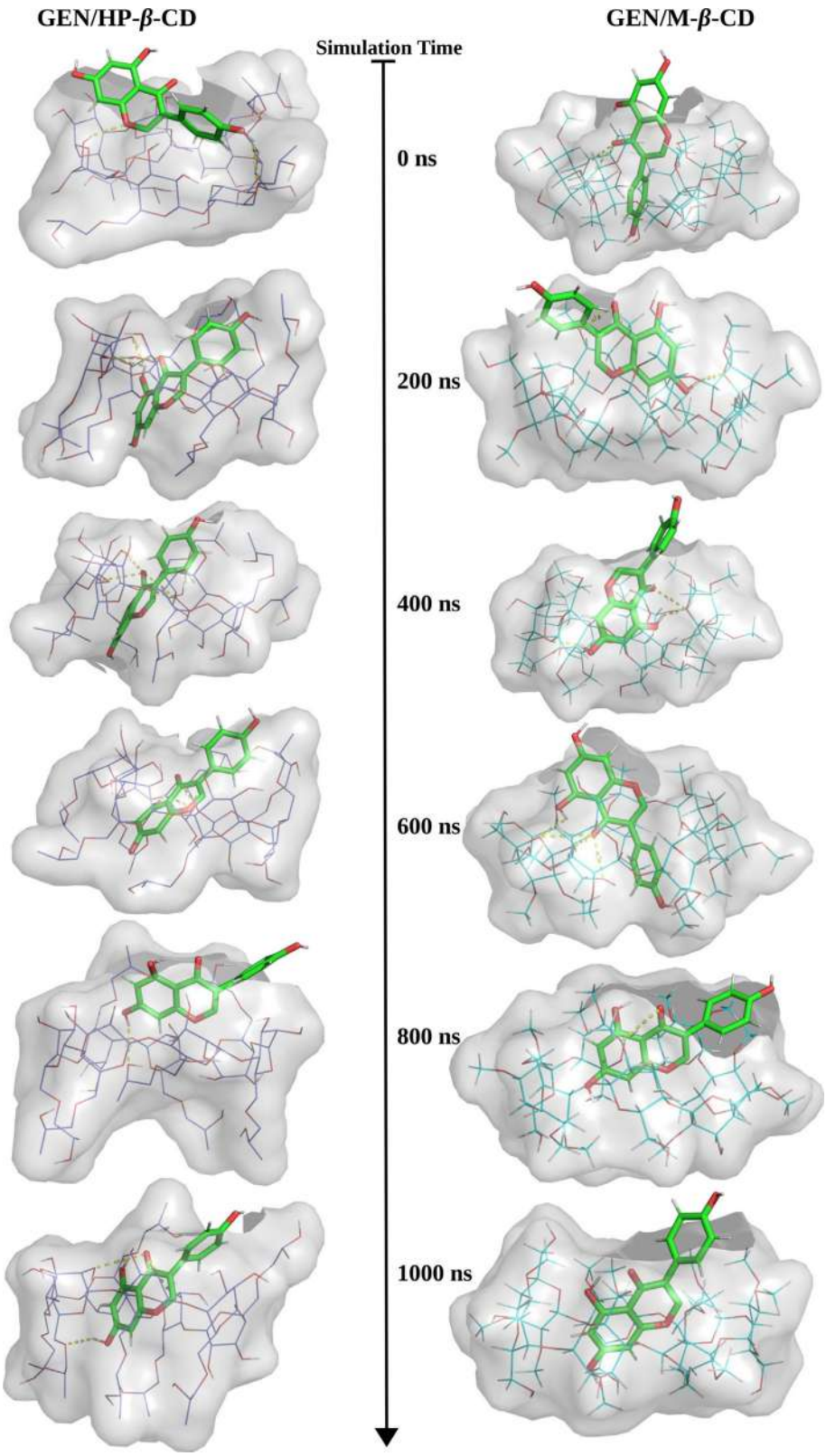

Fig. 6. Analysis of conformational changes in GEN binding with HP-β-CD (left) and M-β-CD (right) at different time intervals (0, 200, 400, 600, 800, and 1000 ns) during MD simulations.

3.7. Analysis of binding poses at different time intervals

Biological processes and structures related to receptor-ligand binding adopt multiple conformations that are linked to their biological functions [94]. The experimental methods including NMR, X-ray crystallography, or electron microscopy can illustrate some of the structural heterogeneity, but are unable to demonstrate the detailed conformational transitions and dynamics [95]. The analysis of intermolecular interactions at different time intervals extracted from the MD trajectories can provide a comprehensive analysis of the receptor-ligand binding dynamics **[**Fig. 6**]**. In the case of GEN/HP-β-CD IC, initially (at 0 ns), GEN interacted with the hydrophilic surface of the HP-β-CD molecule. Thereafter, the chromone ring of GEN entered into the cavity of HP-β-CD and remained inside the hydrophobic core till $\sim$ 800 ns. We observed a change in the binding orientation of GEN at 800 ns which reverted to its stable form at the end of the simulation. These results are consistent with our RMSD analysis where a slight deviation was observed around 800 ns (refer to Fig. 5 (a)). Interestingly, in the case of GEN/M-β-CD IC, GEN showed two orientations inside the hydrophobic core of M-β-CD. The phenyl ring occupied the central cavity of M-β-CD at 0 ns, followed by a shift in orientation at 200 ns, resulting in an IC where the chromone ring occupied the cavity of M-β-CD. Afterward, the phenyl ring reoccupied the central cavity at 600 ns, again followed by a conformation shift that led the chromone ring inside the hydrophobic core of M-β-CD. These results are in perfect sync with our analysis of FEL where we observed two stable conformational states approaching the least energy values (refer to Fig. 5 (c)). The possibility of two orientations of GEN inside the central cavity of unsubstituted β-CD was also explored in a previous study [25]. The strength of interactions between GEN and the substituted forms of β-CD was further analyzed by calculating the free energy through enhanced sampling simulations.

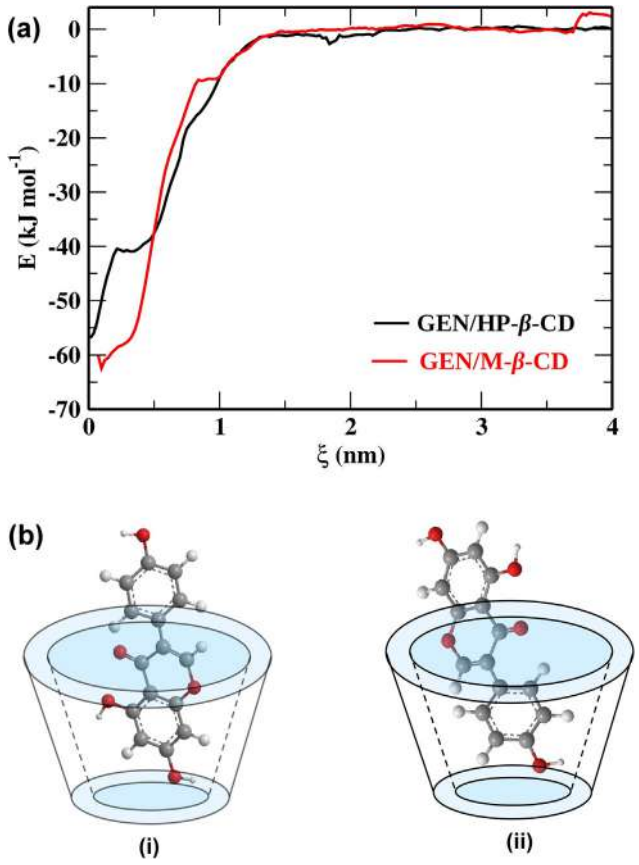

Fig. 7. Potential of mean force (PMF) curves and mode of orientations of GEN inside the cavity of cyclodextrins. (a) A plot showing the potential of mean force (PMF) curves obtained from enhanced umbrella sampling simulations for GEN/HP-β-CD and GEN/M-β-CD complexes and (b) two different modes of orientations of GEN inside the cavity of cyclodextrins, where in case of HP-β-CD (i) orientation was found to be most stable one after MD simulations whereas, in case of M-β-CD both (i and ii) the orientations were found to be stable.

3.8. Determination of binding free energies

The distance between the modified β-CDs and GEN was calculated and selected to represent the reaction coordinate (ξ). The distance was recorded by employing steered MD simulations. The GEN molecule was allowed to move out of the binding site along the z-axis from the HP-β-CD and M-β-CD ICs. A total of 80 sampling windows along the reaction coordinate for both the complexes were subjected to independent biased MD simulations. The weighted histogram analysis method (WHAM) was employed for removing the biasing potential and construction of the potential of mean force (PMF) curves. The GEN/M-β-CD complex achieved the lowest energy value of $-$62.44 kJ/mol at 0.098 nm, while for the GEN/HP-β-CD structure, the minimum energy was $-$56.87 kJ/mol **[**Fig. 7 **(a)]**. The PMF curves were further exploited to extract the change in energy (ΔG) for both the complexes. The ΔG values for HP-β-CD and M-β-CD ICs were $-$57.76 kJ/mol and $-$65.58 kJ/mol respectively. These results indicated that GEN demonstrated stronger interactions with M-β-CD than HP-β-CD structures.

4. Conclusion

In this work, the GEN ICs with modified forms of β-CDs (HP-β-CD and M-β-CD) was successfully prepared by spray-drying technique. Initially, the phase solubility experiment was conducted, which demonstrated that there is a positive correlation between the solubility increment of GEN and CDs concentration (A_L-type curve) with a 1:1 M stoichiometric ratio. The FT-IR, XRD and SEM provided evidences of the inclusion of GEN inside host cavities (CDs). Additionally, SEM micrographs of inclusion complexes reveal no free GEN indicative of the effectiveness of the spray drying method. The molecular inclusion mechanism determined by ^{1}H NMR and 2D NMR showed that the hydroxyphenyl ring and chromone ring were encapsulated into the M-β-CD and HP-β-CD cavity, respectively. Indeed, protons of GEN underwent chemical shift variations after complex formation. Additionally, protons present in the interior of the cavity of CDs (H-3 and H-5) also demonstrated small chemical shift changes due to "non-covalent interactions (hydrogen bonds and van der Waals forces)" with the GEN molecule. In the case of M-β-CD the aromatic ring of GEN was oriented toward the primary rim, while in the case of HP-β-CD, the chromone ring of GEN is entered inside the HP-β-CD cavities from the wider rim edge **[**Fig. 7 **(b)]**.

Moreover, molecular modeling, classical, and enhanced sampling MD simulations based on robust computational analysis elucidated strong interactions between GEN and modified β-CD. Our computational analysis resonated with the experimental findings and showed that GEN formed a compact structure having lower binding free energy with M-β-CD in comparison to complex formed with HP-β-CD. The thoughtful combination of diverse analytical techniques provided particular information on the different binding modes and orientation of the GEN inside the CD cavity. The findings resulting from our approach would be useful and will lay the theoretical foundation for further studies. Moreover, this study represents that the formation of GEN inclusion complexes with M-β-CD can be an effective approach to broaden the application of GEN in functional foods, food supplements and medicinal sectors.

CRediT authorship contribution statement

Nabab Khan: Writing – original draft, Methodology, Formal analysis. **Vijay Kumar Bhardwaj:** Writing – original draft, Methodology, Formal analysis. **Ruchika:** Formal analysis, Writing – original draft. **Rituraj Purohit:** Writing – review & editing, Supervision, Formal analysis. **Ankit Saneja:** Writing – review & editing, Supervision, Project administration, Funding acquisition, Conceptualization.

Data availability

Data will be made available on request.

Declaration of Competing Interest

The authors declare that they have no known competing financial interests or personal relationships that could have appeared to influence the work reported in this paper.

Acknowledgements

The authors are grateful to the Director, CSIR-IHBT, Palampur for his continuous support and encouragement. A.S acknowledges financial assistance from CSIR (MLP204) and SERB, New Delhi (File number: SRG/2020/000141). N.K acknowledges Council of Scientific and Industrial Research (CSIR), New Delhi, for providing Junior Research fellowship (File GATE31/0054(12027)/2021-EMR-I). V.K. B acknowledges Council of Scientific and Industrial Research (CSIR), New Delhi, for providing Senior Research Fellowship (File 31/GATE/54/(07)/2020-EMR-I) and Ruchika acknowledges Council of Scientific and Industrial Research (CSIR), New Delhi, for providing Junior research fellowship (File 31/054(0163)/2020-EMR-I). The Authors acknowledge the Advanced Materials Research Center, Indian Institute of Technology, Mandi for carrying out PXRD analyses. The manuscript bears institutional communication number 5127.

Appendix A. Supplementary material

Supplementary data to this article can be found online at https://doi.org/10.1016/j.molliq.2023.121295.

References

[1] R.K. Dhritlahre, Y.S. Ruchika, A. Saneja Padwad, Trends Food Sci. Technol. 115 (2021) 347.
[2] X. Xin, C. Chen, Y.-Y. Hu, Q. Feng, Biomed. Pharmacother. 117 (2019).
[3] F. Nazari-Khanamiri, M. Ghasemnejad-Berenji, J. Food Biochem. 45 (2021) e13972.
[4] C. Danciu, C. Soica, E. Csanyi, R. Ambrus, S. Feflea, C. Peev, C. Dehelean, Chem. Cent. J. 6 (2012) 58.
[5] A. Zafar, N.K. Alruwaili, S.S. Imam, O.A. Alsaidan, F.K. Alkholifi, K.S. Alharbi, E.M. Mostafa, A.S. Alanazi, S.J. Gilani, A. Musa, S. Alshehri, A. Rawaf, A. Alquraini, Pharmaceutics 13 (2021) 1997.
[6] B. dos Santos Lima, S. Shanmugam, J. de Souza Siqueira, L.J. Quintans, A.A. de Quintans-Júnior, S. Araújo, Phytochem. Rev. 18 (2019) 1337.
[7] D. Arora, A. Saneja, S. Jaglan, Environ. Chem. Lett. 17 (2019) 1263.
[8] Y. Hu, C. Qiu, Y. Qin, X. Xu, L. Fan, J. Wang, Z. Jin, Trends Food Sci. Technol. 109 (2021) 398.
[9] M.E. Davis, M.E. Brewster, Nat. Rev. Drug Discov. 3 (2004) 1023.
[10] G. Varan, C. Varan, N. Erdoğar, A.A. Hıncal, E. Bilensoy, Int. J. Pharm. 531 (2017) 457.
[11] A. Vyas, S. Saraf, S. Saraf, J. Incl. Phenom. Macrocycl. Chem. 62 (2008) 23.
[12] M. Jug, in: Nanomaterials for Clinical Applications, Elsevier, 2020, pp. 29–69.
[13] V. Suvarna, P. Gujar, M. Murahari, Biomedicine & pharmacotherapy = Biomedecine & pharmacotherapie 88 (2017) 1122.
[14] Y. Liu, D.E. Sameen, S. Ahmed, Y. Wang, R. Lu, J. Dai, S. Li, W. Qin, Food Chem. 370 (2022).
[15] P. Han, Y. Zhong, N. An, S. Lu, Q. Wang, J. Dong, J. Mol. Liq. 339 (2021).
[16] Y. Wei, J. Zhang, A.H. Memon, H. Liang, J. Mol. Liq. 236 (2017) 68.
[17] S. Li, L. Yuan, Y. Chen, W. Zhou, X. Wang, Molecules (Basel, Switzerland) 22 (2017).
[18] B. Tian, D. Xiao, T. Hei, R. Ping, S. Hua, J. Liu, Polym. Int. 69 (2020) 597.
[19] J. Wankar, N.G. Kotla, S. Gera, S. Rasala, A. Pandit, Y.A. Rochev, Advanced Functional Materials 30 (2020) 1909049.
[20] Y. Wang, Z. Deng, X. Wang, Y. Shi, Y. Lu, S. Fang, X. Liang, International Journal of Pharmaceutics 603 (2021) 120696.
[21] V. Crupi, R. Ficarra, M. Guardo, D. Majolino, R. Stancanelli, V. Venuti, Journal of pharmaceutical and biomedical analysis 44 (2007) 110.
[22] V. Crupi, D. Majolino, A. Paciaroni, B. Rossi, R. Stancanelli, V. Venuti, G. Viliani, J. Raman Spectrosc. 41 (2010) 764.
[23] C. Cannavà, V. Crupi, P. Ficarra, M. Guardo, D. Majolino, A. Mazzaglia, R. Stancanelli, V. Venuti, J. Pharm. Biomed. Anal. 51 (2010) 1064.
[24] C. Danciu, C. Soica, M. Oltean, S. Avram, F. Borcan, E. Csanyi, R. Ambrus, I. Zupko, D. Muntean, C.A. Dehelean, M. Craina, R.A. Popovici, Int. J. Mol. Sci. 15 (2014) 1962.
[25] C. Hanpaibool, T. Chakcharoensap, Y. Arifin, S. Hijikata, P. Irle, N. Wolschann, P. Kungwan, P. Pongsawasdi, T.R. Ounjai, J. Mol. Liq. 265 (2018) 16.
[26] V. Venuti, C. Corsaro, R. Stancanelli, A. Paciaroni, V. Crupi, S. Tommasini, C.A. Ventura, D. Majolino, Chem. Phys. 516 (2019) 125.
[27] N. Bansal, Z. Zheng, D.S. Cerutti, K.M. Merz, J. Comput. Aided Mol. Des. 31 (2017) 47.
[28] W. You, Z. Tang, C.A. Chang, J. Chem. Theory Comput. 15 (2019) 2433.
[29] S.C. Hu, Y.C. Lai, C.L. Lin, W.S. Tzeng, F.L. Yen, Phytomedicine : international journal of phytotherapy and phytopharmacology 57 (2019) 174.
[30] T. Higuchi and K. A. Connors, In: C. N. Reilly, Ed., Advances in Analytical Chemistry and Instrumentation, 4 (1965) 117.
[31] C. Tamames-Tabar, E. Imbuluzqueta, M.A. Campanero, P. Horcajada, M.J. Blanco-Prieto, J. Chromatogr. B 935 (2013) 47.
[32] M.I. Rodríguez-López, M.T. Mercader-Ros, S. López-Miranda, J.A. Pellicer, A. Pérez-Garrido, H. Pérez-Sánchez, E. Núñez-Delicado, J.A. Gabaldón, J. Sci. Food Agric. 99 (2019) 1322.
[33] P.N. de Melo, E.G. Barbosa, C. Garnero, L.B. de Caland, M.F. Fernandes-Pedrosa, M.R. Longhi, A.A. da Silva-Júnior, J. Mol. Liq. 223 (2016) 350.
[34] B.R. Giri, J. Lee, D.Y. Lim, D.W. Kim, Drug Dev. Ind. Pharm. 47 (2021) 319.
[35] A. Cid-Samamed, J. Rakmai, J.C. Mejuto, J. Simal-Gandara, G. Astray, Food Chem. 384 (2022).
[36] M.M. Anjum, K.K. Patel, N. Pandey, R. Tilak, A.K. Agrawal, S. Singh, J. Mol. Liq. 296 (2019).
[37] Y. Wu, Y. Xiao, Y. Yue, K. Zhong, Y. Zhao, H. Gao, Food Hydrocoll. 103 (2020).
[38] S. Kim, J. Chen, T. Cheng, A. Gindulyte, J. He, S. He, Q. Li, B.A. Shoemaker, P.A. Thiessen, B. Yu, L. Zaslavsky, J. Zhang, E.E. Bolton, Nucleic Acids Res. 49 (2020) D1388.
[39] D.J.A.S.I. Studio, (2015) 98.
[40] D. Van Der Spoel, E. Lindahl, B. Hess, G. Groenhof, A.E. Mark, H.J. J. J. o.c.c. Berendsen,, J. Comput. Chem. 26 (2005) 1701.
[41] B. Hess, C. Kutzner, D., Van Der Spoel, E.J.J.o.c.t. Lindahl, computation, J. Chem. Theory Comput. 4 (2008) 435.
[42] M.J. Abraham, T. Murtola, R. Schulz, S. Páll, J.C. Smith, B. Hess, E.J.S. Lindahl, SoftwareX 1 (2015) 19.
[43] A.W. Schüttelkopf, D.m.j.a.c.s.d.b.c., Van Aalten, Acta Crystallogr. 60 (2004) 1355.
[44] M.J.J.o.A.P. Parrinello, Journal of Applied Physics 52 7182.
[45] H.J. Berendsen, J.v. Postma, W.F. Van Gunsteren, A. DiNola, J.R.J.T.J.o.c.p. Haak,, J. Chem. Phys. 81 (1984) 3684.
[46] V. Kräutler, W.F. Van Gunsteren, P.H.J.J.o.c.c. Hünenberger,, J. Comput. Chem. 22 (2001) 501.
[47] U. Essmann, L. Perera, M. Berkowitz, T. Darden, H.J.A.s.p.m.E.m. Lee,, J. Chem. Phys. 103 (1995) 8577.
[48] J.J.W.I.R.C.M.S. Kästner, 1 (2011) 932.
[49] S. Kumar, J.M. Rosenberg, D. Bouzida, R.H. Swendsen, P.A. Kollman, J. Comput. Chem. 13 (1992) 1011.
[50] R. Li, J. Hao, H. Fujiwara, M. Xu, S. Yang, S. Dai, Y. Long, M. Swaroop, C. Li, M. Vu, J.J. Marugan, D.S. Ory, W. Zheng, Assay Drug Dev. Technol. 15 (2017) 154.
[51] X. Hu, Z. Zhou, L. Han, S. Li, W. Zhou, New J. Chem. 44 (2020) 5218.
[52] R. Stancanelli, V. Venuti, A. Arigò, M.L. Calabrò, C. Cannavà, V. Crupi, D. Majolino, S. Tommasini, C.A. Ventura, J. Incl. Phenom. Macrocycl. Chem. 83 (2015) 27.
[53] S. Jacob, A.B. Nair, Drug Dev. Res. 79 (2018) 201.
[54] P. Saokham, C. Muankaew, P. Jansook, T. Loftsson, Molecules (Basel, Switzerland) 23 (2018).
[55] Z. Xiao, Y. Zhang, Y. Niu, Q. Ke, X. Kou, Carbohydr. Polym. 269 (2021).
[56] F. Chen, J. Peng, D. Lei, J. Liu, G. Zhao, Food Sci. Human Wellness 2 (2013) 124.
[57] P.S. Santos, L.K.M. Souza, T.S.L. Araújo, J.V.R. Medeiros, S.C.C. Nunes, R.A. Carvalho, A.C.C. Pais, F.J.B. Veiga, L.C.C. Nunes, A. Figueiras, ACS Omega 2 (2017) 9080.
[58] C. Yuan, B. Liu, H. Liu, Carbohydr Polym 118 (2015) 36.
[59] A. Garg, J. Ahmad, M.Z. Hassan, J. Drug Delivery Sci. Technol. 64 (2021).
[60] S. Gao, Y. Liu, J. Jiang, X. Li, F. Ye, Y. Fu, L. Zhao, Colloids Surf. B Biointerfaces 201 (2021).
[61] S. Gao, X. Li, J. Jiang, L. Zhao, Y. Fu, F. Ye, J. Mol. Liq. 335 (2021).
[62] J.A. da Silva, P.A. Sampaio, L.J.L. Dulcey, M.R. Cominetti, M.M. Rabello, L.A. Rolim, J. Drug Delivery Sci. Technol. 61 (2021).
[63] M. Soleimanpour, A.M. Tamaddon, M. Kadivar, S.S. Abolmaali, H. Shekarchizadeh, Int. J. Biol. Macromol. 159 (2020) 1031.
[64] S. Gao, C. Bie, Q. Ji, H. Ling, C. Li, Y. Fu, L. Zhao, F. Ye, RSC Adv. 9 (2019) 26109.

[65] O. Adeoye, C. Costa, T. Casimiro, A. Aguiar-Ricardo, H. Cabral-Marques, J. Supercrit. Fluids 133 (2018) 479.
[66] M.P. Kapoor, M. Moriwaki, M. Ozeki, D. Timm, Carbohydrate Polymer Technologies and Applications 2 (2021).
[67] Y. Liu, Y. Chen, X. Gao, J. Fu, L. Hu, Crit. Rev. Food Sci. Nutr. 62 (2022) 2627.
[68] C. Xavier, A. Silva, L. Schwingel, G. Borghetti, L. Koester, P. Mayorga, H. Teixeira, V. Bassani, I. Lula, R. Sinisterra, Quimica Nova - QUIM NOVA 33 (2010).
[69] E.U. Stolarczyk, K. Stolarczyk, M. Łaszcz, M. Kubiszewski, W. Maruszak, W. Olejarz, D. Bryk, Eur. J. Pharm. Sci. 96 (2017) 176.
[70] C. Yuan, Z. Jin, X. Xu, Carbohydr. Polym. 89 (2012) 492.
[71] S. Goswami, M. Sarkar, New J. Chem. 42 (2018) 15146.
[72] J.M. Bezamat, F. Yokaichiya, M.K.K. Dias Franco, S.R. Castro, E. de Paula, L.F. Cabeça, J. Drug Delivery Sci. Technol. 55 (2020).
[73] P. Tang, L. Wang, X. Ma, K. Xu, X. Xiong, X. Liao, H. Li, AAPS PharmSciTech 18 (2017) 104.
[74] L. Wang, S. Li, P. Tang, J. Yan, K. Xu, H. Li, Carbohydr. Polym. 129 (2015) 9.
[75] Y. Yao, Y. Xie, C. Hong, G. Li, H. Shen, G. Ji, Carbohydr Polym 110 (2014) 329.
[76] A. Sedaghat Doost, M. Akbari, C.V. Stevens, A.D. Setiowati, P. Van der Meeren, Trends Food Sci. Technol. 86 (2019) 16.
[77] D. Neuhaus, M.P. Williamson, The nuclear Overhauser effect in structural and conformational analysis 1989.
[78] F. Pessine, A. Calderini, G. Alexandrino, Magnetic Resonance Chemistry, 2012.
[79] P. Mura, J. Pharm. Biomed. Anal. 101 (2014) 238.
[80] C. Deng, C. Cao, Y. Zhang, J. Hu, Y. Gong, M. Zheng, Y. Zhou, Food Hydrocoll. 123 (2022).
[81] T. Gratieri, L.A.G. Pinho, M.A. Oliveira, L.L. Sa-Barreto, R.N. Marreto, I.C. Silva, G. M. Gelfuso, J. de Souza Siqueira, L.J. Quintans, M.-F. Quintans-Junior, Carbohydr Polym 231 (2020).
[82] L.-J. Yang, S.-X. Ma, S.-Y. Zhou, W. Chen, M.-W. Yuan, Y.-Q. Yin, X.-D. Yang, Carbohydr. Polym. 98 (2013) 861.
[83] Y. Inoue, M. Yoshida, T. Ezawa, T. Tanikawa, F. Arce Jr., G.L. See, J. Tomita, M. Suzuki, T. Oguchi, AAPS PharmSciTech 23 (2021) 2.
[84] R. Zhao, C. Sandström, H. Zhang, T. Tan, Molecules (Basel, Switzerland) 21 (2016) 372.
[85] W. Wu, Y. Zu, X. Zhao, X. Zhang, L. Wang, Y. Li, L. Wang, Y. Zhang, B. Lian, Drug Dev. Ind. Pharm. 43 (2017) 1366.
[86] M. Jafar, M.S. Khalid, H. Alghamdi, M. Amir, S.A. Al Makki, O.S. Alotaibi, A.A. Al Rmais, S.S. Imam, S. Alshehri, S.J. Gilani, AAPS PharmSciTech 23 (2022) 71.
[87] J.-Q. Zhang, K.-M. Jiang, K. An, S.-H. Ren, X.-G. Xie, Y. Jin, J. Lin, Carbohydr. Res. 418 (2015) 20.
[88] J. Chao, J. Su, J. Li, W. Zhao, S. Huang, R. Du, Supramol. Chem. 23 (2011) 641.
[89] M.Y. Lobanov, N.S. Bogatyreva, O.V. Galzitskaya, Mol. Biol. 42 (2008) 623.
[90] T.A. Collier, T.J. Piggot, J.R. Allison, Methods in molecular biology (Clifton, N.J.) 2073 (2020) 311.
[91] R. Singh, S. Kumar, V.K. Bhardwaj, R.J. Purohit, J. Mol. Liq. 358 (2022).
[92] X. Wu, Q. Hu, X. Liang, S. Fang, Food Chem. 391 (2022).
[93] Y. Dai, J. Zhong, J. Li, X. Liu, Y. Wang, X. Qin, Food Hydrocoll. 130 (2022).
[94] G. Anderson, J. Dupré, J.G. Wakefield, eLife 8 (2019) e46962.
[95] R. Shukla, T. Tripathi, Computer-aided drug design, Springer, 2020, pp. 133–161.

Journal of Molecular Liquids 391 (2023) 123348

Contents lists available at ScienceDirect

Journal of Molecular Liquids

journal homepage: www.elsevier.com/locate/molliq

Unveiling the complexation mechanism of phloretin with Sulfobutylether–β–cyclodextrin (Captisol®) and its impact on anticancer activity

Nabab Khan [a,b], Garima Slathia [a], Ankit Saneja [a,b,*]

[a] Formulation Laboratory, Dietetics and Nutrition Technology Division, CSIR-Institute of Himalayan Bioresource Technology, Palampur 176061, Himachal Pradesh, India
[b] Academy of Scientific and Innovative Research (AcSIR), Ghaziabad, 201002, India

ARTICLE INFO

Keywords:
Phloretin
Solubility
Sulfobutylether-β-cyclodextrin
Molecular interactions
Inclusion complex
Anticancer

ABSTRACT

The incorporation of phloretin (PHL), a dihydrochalcone flavonoid, in functional foods is usually hampered by its low aqueous solubility. In this regard, we investigated the impact of complexation of PHL with sulfobutylether-β-cyclodextrin (SBE-β-CD, Captisol®) to overcome its limitation. The phase solubility studies of PHL with different β-CDs derivatives represents A_L-type of curve where, SBE-β-CD demonstrated highest apparent stability constant (Ks: 15,856 M^{-1}) indicating its strong affinity to form host-guest assembly. Solid-state characterizations (including SEM, FT-IR, PXRD, DSC, TGA) provided direct evidences of inclusion complex (IC) formation. The detailed molecular interaction between the host–guest assembly was performed using ^{1}H NMR and 2D-NOESY revealed that protons of aromatic phenyl ring of PHL (guest) molecule exhibit direct correlation with the protons lying in the inner cavity of SBE-β-CD (host). Furthermore, the anticancer potential of PHL/SBE-β-CD-IC was examined using cytotoxicity studies, caspase 3/7 activation assay, reactive oxygen species (ROS) generation and disturbance in mitochondrial membrane potential (MMP) in lung carcinoma cell line (A549) and human pancreatic cancer cell line (MiaPaCa–2). The *in-vitro* cytotoxicity assay on both cell lines demonstrated higher antiproliferative activity of IC as compared to free PHL in concentration dependent manner. In addition, it was found that PHL/SBE-β-CD-IC induces apoptosis via activation of caspase 3/7, reactive oxygen species generation and inducing depolarization of mitochondrial membrane potential in both the cell lines (MiaPaCa–2 and A549). Overall, the study provides a promising approach to enhance the solubility and bioactivity of PHL utilizing SBE-β-CD inclusion complexation.

1. Introduction

Phloretin, (PHL) [3-(4-hydroxyphenyl)-1-(2,4,6-trihydroxyphenyl) propan-1-one], a crystalline dihydrochalcone naturally obtained from apples, kumquats, pears, and strawberries [1,2]. It exerts panoply of pharmacological effects (including regulation of glucose transporters, free radical scavenging, and strong ability to induce apoptosis in tumor cells) due to its unique chemical structure that consist of two aromatic phenol rings (ring A and B), four hydroxyl and a carbonyl group [3–5]. Despite of its tremendous biological properties the application of PHL in food industry is constrained by its poor aqueous solubility (<0.2 mM), unfavorable metabolism and rapid elimination which ultimately impedes its therapeutic potential [6].

In order to tackle these technological challenges, various solubility enhancement approaches have been investigated in past few years including solid dispersions, nanoparticles, nanoemulsions, nanostructured lipid carriers and electrospun nanofibers [1,2,6–9]. In this regard, the development of cyclodextrin (CDs) inclusion complex (IC) (host–guest assembly) have gained tremendous attention in ameliorating the solubility, stability, permeability, and dissolution profile of poorly aqueous soluble bioactive molecules leading to an improved bioaccessibility and better therapeutic efficacy [10,11].

Among the three natural (first-generation) forms of CDs (α, β, and γ), the β-CD is the most extensively used due to its inexpensive price and wide availability. However, β-CD is associated with renal toxicity and hemolytic effects. Moreover, its limited water solubility (1.85 g/100 mL

* Corresponding author.
E-mail addresses: ankitsaneja@ihbt.res.in, ankitsaneja.ihbt@gmail.com (A. Saneja).

https://doi.org/10.1016/j.molliq.2023.123348
Received 15 August 2023; Received in revised form 6 October 2023; Accepted 12 October 2023
Available online 14 October 2023

at 25 °C) results in formation of insoluble complexes due to precipitation of incorporated bioactive molecules [12,13]. To overcome these obstacles, natural β-CD is modified with several moieties such as methyl (M), hydroxypropyl (HP) and sulfobutylether (SBE) to produce M-β-CD, HP-β-CD and SBE-β-CD derivatives, respectively [14]. The SBE-β-CD is non-toxic (no signs of nephrotoxicity and low tendency to cause hemolysis), biocompatible, possesses higher aqueous solubility [(70 g/100 mL at 25 °C) ~ 40 folds higher compared to native β-CD] and confers improved binding capability as compared to the native β-CD [15–17]. SBE-β-CD is marketed under the trade name Captisol® and was first manufactured by CyDex (now a division of Ligand Pharmaceuticals Inc.) [18]. It is an USFDA approved excipient and till date there are more than 15 Captisol® enabled products that have gained FDA approval for commercialization [16].

In the present investigation, we have prepared PHL inclusion complex with SBE-β-CD via lyophilization process. As a preliminary screening step, to find out the molar stoichiometric ratio and apparent binding potential of host with guest molecules, phase solubility experiment was conducted with different derivatives of β-CD *viz.* M-β-CD, HP-β-CD and SBE-β-CD. Phase solubility studies led to the selection of SBE-β-CD, and the IC of PHL was produced using SBE-β-CD at a (1:1) molar stoichiometric ratio [Fig. 1]. The successful formation of IC was confirmed *via* different solid-state characterizations (such as SEM, FT-IR, PXRD and thermal analysis). Moreover, to delve deeper insights on host and guest intermolecular interactions, proton nuclear magnetic resonance (^{1}H NMR) and 2 – dimensional nuclear overhauser effect spectroscopy (2D NOESY) has been carried out. The *in vitro* dissolution profile of PHL and PHL/SBE-β-CD-IC has also been investigated to observe the solubilization effect. Finally, the impact of PHL/SBE-β-CD-IC on cell proliferation, caspase3/7 activation, reactive oxygen species (ROS) generation and mitochondrial membrane potential (MMP) depolarization in two different cancer cell lines (A549 and MiaPaCa-2) was investigated.

To the best of our knowledge, the inclusion complex of SBE-β-CD and PHL has not yet been investigated and therefore, this study opens the avenues for exploring the SBE-β-CD based inclusion complexes for enhancing the solubility and biological activity of PHL.

2. Materials and methods

Phloretin ($C_{15}H_{14}O_5$, Mw: 274.27 g/mol, greater than 98.0 % Purity, Cas No. 60–82–2) was purchased from TCI chemicals. Methyl-β-cyclodextrin (Average Mn: 1310, Cas No: 128446–36-6), (2-Hydroxypropyl)-β-cyclodextrin (Average Mn: ~1460 g/mol, Cas No. 128446–35-5), Deuterium oxide ("100 %", ≥ 99.96 atom % D, Cas No. 7789–20–0), DMSO-d_6 ("100 %", ≥ 99.96 atom % D, contains 0.03 % (v/v) TMS, Cas No. 2206–27–1) were purchased from Sigma-Aldrich. Sulfobutylether-β-cyclodextrin (Captisol®, n = 6.6, Cas No. 182410–00-0) was offered as gift sample from CyDex Pharmaceuticals Inc. (Kansas, USA). Unless otherwise stated, analytical grades chemicals and reagents were used for experiments.

2.1. Quantitative analysis of PHL

The quantitative analysis of PHL was performed using Agilent HPLC (Agilent 1260 Infinity II, Waldbronn, Germany) equipped with quaternary pump (G7111A, 1260 Quat pump VL), an automatic vial sampler injector (G7129A, 1260 Vial sampler), a multicolumn thermostat (G7116A, 1260 MCT), and a DAD detector (G7115A, 1260 DADWR). The C18 reverse phase column (LiChrospher® 100 RP-18 Hibar® RT 250 mm × 4.6 mm, 5 μm, Darmstadt, Germany) was used for the chromatographic separation. The samples were eluted in isocratic mode at 1 mL/min. flow rate using mobile phase composed of [Eluent A: Acetonitrile; Eluent B: Water (0.01 % TFA), (45:55 v/v)]. The detection of PHL was carried out at preset wavelength of 286 nm [19].

2.2. Determination of molar stoichiometry and apparent stability constant

The phase solubility study of PHL was carried out with three modified derivatives of cyclodextrins [i.e., Methyl-β-cyclodextrin (M-β-CD), (2-Hydroxyproyl)-β-cyclodextrin (2-HP)-β-CD and Sulfobutylether-β-cyclodextrin (SBE-β-CD)]. The experiment was conducted accordingly as per Higuchi and Connors with slight modifications [20]. A series of aqueous solutions of M-β-CD, (2-HP)-β-CD and SBE-β-CD (0 to 20 mM) were prepared separately in 2 mL microcentrifuge tubes. Then, a surplus amount of PHL was added in each tube. The resulting suspension were placed in IKA® matrix orbital shaker (Delta F2.0, Germany) for 48 h in

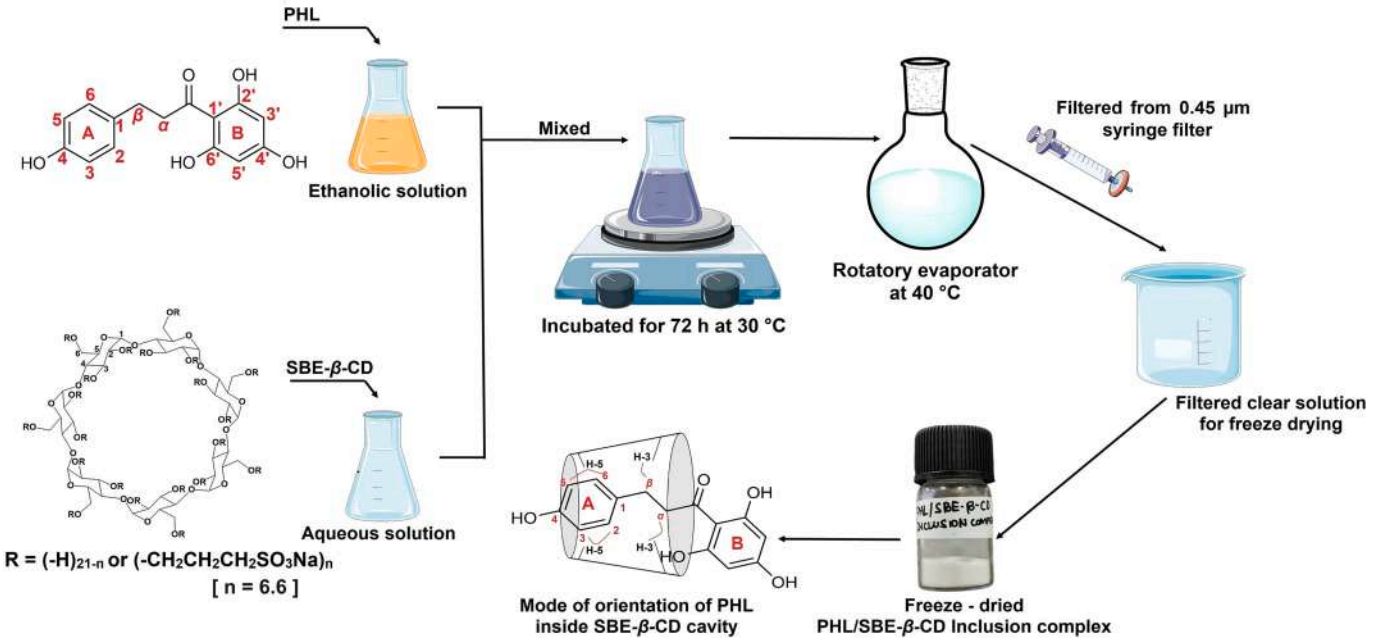

Fig. 1. Schematic illustration of concept of study representing structure of phloretin and sulfobutylether-β-cyclodextrin, method of preparation of PHL/SBE-β-CD inclusion complex *via* lyophilization technique and mode of orientation of phloretin inside SBE-β-CD cavity (elucidated from 2D-NMR technique).

dark at controlled temperature (37 °C) with constant shaking. The obtained solution was centrifuged (12,000 rpm; 15 min.) and supernatant was filtered through syringe filter (0.45 μm; Millipore Millex-HV, PVDF) to remove the undissolved PHL. The capacity of cyclodextrins to solubilize PHL was analyzed using HPLC method as described in Section 2.1.

The phase solubility graph was plotted between the molar concentration of CDs *versus* the molar concentration of PHL on *x* and *y*-axis, respectively. The apparent stability constant (Ks) of different cyclodextrins towards PHL was calculated by Higuchi-Connor's equation:

$$Ks = \left[\frac{slope}{S_0(1 - slope)}\right]$$

where, S_0 denotes intrinsic solubility of PHL (solubility in absence of CDs), and slope value was obtained from the phase solubility linear curves. The experiments were performed in triplicates and data were presented as mean ± SD (n = 3).

2.3. Preparation of PHL/SBE-β-CD inclusion complex (IC)

On the basis of our phase solubility experiment, we have chosen SBE-β-CD as it demonstrated maximum solubility and apparent stability constant and therefore, PHL inclusion complex with SBE-β-CD was developed in a 1:1 M stoichiometric ratio (PHL:SBE-β-CD). Briefly, PHL was dissolved in 12 mL ethanol (20 mM, 0.22 g) and SBE-β-CD (20 mM, 1.21 g) was dissolved in 28 mL of Milli-Q water. Both the solutions were mixed and incubated for 72 h at 30 °C on magnetic stirrer. Afterward, vacuum distillation at 40 °C using rotatory evaporator (IKA® RV 10) was carried out to remove the ethanol from the solution mixture. The obtained solution was filtered through 0.45 μm syringe filter (Millipore Millex-HV, PVDF)and lyophilized using freeze-dryer (Labonco, FreezeZone, Kansas City, MO, USA) [21]. The obtained PHL/SBE-β-CD-IC was stored in air-sealed container at cool place.

2.4. Preparation of PHL/SBE-β-CD physical mixture (PM)

For comparative studies, the physical mixture (PM) of PHL with SBE-β-CD was obtained by simple blending of PHL: SBE-β-CD (1:1 molar ratio) in a ceramic mortar pestle for 15–20 min and obtained mixture powder was sieved, stored in tight sealed vials [22].

2.5. Characterization of PHL/SBE-β-CD inclusion complex (IC)

2.5.1. Determination of embedding efficiency (EE) and loading efficiency (LE)

The percentage embedding efficiency (EE) and loading efficiency (LE) was determined as per previously reported method with appropriate modifications [23]. First, 10 mg of PHL/SBE-β-CD-IC was dissolved in 1 mL of milli-Q water and placed in IKA® matrix orbital shaker for 48 h at 37 °C. The obtained solution was centrifuged at 12,000 rpm for 15 min and supernatant was collected and filtered through syringe filter 0.45 μm (Millipore Millex-HV, PVDF) to remove the undissolved PHL. The PHL was quantified using HPLC system as per the method described in section 2.1. The calculations have been performed using following equations:

$$EE\% = \frac{(Amount\ of\ PHL\ in\ inclusion\ complex)}{(Initial\ amount\ of\ PHL\ added)} \times 100$$

$$LE\% = \frac{(Amount\ of\ PHL\ in\ inclusion\ complex)}{(Amount\ of\ inclusion\ complex)} \times 100$$

2.5.2. Surface morphology analysis

The surface morphology of the specimens (PHL, SBE-β-CD, PM, and PHL/SBE-β-CD-IC) were visualized via scanning electron microscope (S-3400 N SEM, Hitachi, Tokyo, Japan). Prior to examination, a two-step sample preparation procedure was followed: firstly, the samples were spread over brass stub with the aid of double-sided carbon adhesive tape. In the second step, to avail the good electrical conductivity during microscopic scans, samples were coated with gold using ion sputter coater (Hitachi, E-1010) under an argon atmosphere. An accelerating voltage of 15 kV was used for carrying out imaging of the samples.

2.5.3. Fourier transform infrared spectroscopy (FT-IR)

The FT-IR spectrophotometer (PerkinElmer, USA, with software spectrum ES version 10.5.3) was used to acquire the FT-IR spectra of PHL, SBE-β-CD, PHL/SBE-β-CD-IC and corresponding PM. The materials were mixed with potassium bromide (KBr) and then compressed using a hydraulic press to create KBr pellets. The spectrum was acquired with a resolution of 4 cm^{-1} in the spectral range of 4000 cm^{-1} and 500 cm^{-1}.

2.5.4. Recording of X-ray powder diffractometry (PXRD) pattern

The PXRD patterns of powdered samples were examined using smartLab 9 kW rotating anode X-ray diffractometer (Rigaku Corporation, Tokyo, Japan) equipped with a Cu-Kα radiation source. The instrumental analysis was performed at applied current of 40 mA and voltage of 40 kV. The patterns were acquired as per mentioned parameters - diffraction angle (2θ): 5° to 60°, scan rate: 10°/min and step size: 0.2°.

2.5.5. Unveiling the mode of orientation through 1D and 2D – Nuclear magnetic resonance (NMR) spectroscopy analysis

^{1}H NMR spectra of the PHL, SBE-β-CD, and PHL/SBE-β-CD-IC as well as 2D-NOESY spectra of PHL/SBE-β-CD-IC were obtained in order to get deeper insight on the intermolecular interaction between the SBE-β-CD (host) and PHL (guest) molecules. The experimental parameters used to acquire the 2D-NOESY were 64 scans, 0.18 second for acquisition, and 2.0 seconds for relaxation. NMR spectra were recorded on 500 MHz NMR spectrometer (AV-500, Bruker, Switzerland) at room temperature using D_2O/DMSO-d_6 (600 μL) as NMR solvent. The chemical shift was expressed in terms of parts per million (ppm) and changes in chemical shifts (Δδ) were calculated using following equation:

$$\textbf{\textit{Chemical shift changes}}(\Delta\boldsymbol{\delta}) = \boldsymbol{\delta}_{(complex)} - \boldsymbol{\delta}_{(free)}$$

2.5.6. Differential scanning calorimetry (DSC) analysis

The thermal behavior was analyzed using differential scanning calorimeter (DSC200, Hitachi). The DSC thermograms were acquired at a heating rate of 10 °C per minute and recorded in the range of 25 °C to 300 °C, under a dynamic nitrogen flow (50 mL/min). The samples were hermetically sealed in chromated aluminum pan containing approximately 3 – 5 mg of the samples and empty sealed chromated aluminum pan served as reference [8].

2.5.7. Thermal gravimetric analysis (TGA)

The thermal degradation curves of PHL, SBE-β-CD, PM and PHL/SBE-β-CD-IC were analyzed using TGA thermal analyzer (Mettler Toledo, model: TGA/DSC-I, Columbus, OH, USA). The thermal degradation curves were acquired at heating rate of 10 °C/min over the temperature range from 25 °C to 700 °C, under dynamic nitrogen atmosphere.

2.5.8. In vitro dissolution test

The dissolution of pure PHL and PHL/SBE-β-CD-IC (equivalent to 20 mg PHL) was assessed using the USP apparatus II (*in vitro* dissolution apparatus, Lab India DS 8000, India) as per the procedure carried out by Pal *et. al.* with slight modifications [24]. Briefly, the dissolution chamber filled with 900 mL of phosphate buffer (pH 7.2) maintained at 37 °C ± 0.5 °C with paddle rotation of 100 ± 2 rpm to simulate physiological conditions. The samples were filled in capsules and placed in dissolution chamber with aid of sinker. At specified time intervals (0, 30, 60, 90 and 120 min), 5 mL aliquots were withdrawn and to maintain the sink condition, subsequent replacement was done by adding 5 mL of freshly prepared dissolution media (pH 7.2 phosphate buffer) to the chamber.

The collected sample aliquots were filtered using membrane filter 0.45 μm syringe filter (Millipore Millex-HV, PVDF) and the filtrates were quantified for PHL content using HPLC system.

2.6. Anti-tumor activity of PHL/SBE-β-CD inclusion complex (IC)

2.6.1. Cell culture and its maintenance

The cell lines [Human pancreatic cancer cell line (MiaPaCa–2) and lung carcinoma cell line (A549)] were procured from the National Centre for cell science (NCCS), Pune, INDIA. The cancer cell lines were grown in tissue culture flasks in complete DMEM, High glucose medium (Hi-Media) supplemented with 10 % (v/v) fetal bovine serum (MP Biomedicals), 1X antibiotic- antimycotic (Gibco) in 5 % CO_2 at 37 °C in 95 % humidified atmosphere. For cell viability assay, the cells were treated with various concentration (i.e., 10, 50, 100, 200 and 300 μM) of PHL and PHL/SBE-β-CD-IC (equivalent to PHL amount) and for remaining experiments, cells were treated with 100, 150 and 200 μM PHL and PHL/SBE-β-CD-IC (equivalent to PHL amount) concentration.

2.6.2. Evaluation of PHL/SBE-β-CD-IC effect on cell viability of MiaPaCa–2 and A549

The cytotoxic effect of PHL, SBE-β-CD and PHL/SBE-β-CD-IC on pancreatic cancer cells (MiaPaCa–2) and lung cancer cells (A549) was evaluated using cell counting kit (CCK-8, Sigma-Aldrich) assay [25]. Briefly, both type of cells (MiaPaCa–2 & A549) were seeded at 5×10^3 cells density per well in 96 well cell plate separately and incubated for 24 h at 37 °C. The cells were treated with various concentrations of PHL and PHL/SBE-β-CD-IC (as mentioned earlier in Section 2.6.1) and further incubated for 24 h in CO_2 incubator. Following the incubation period, 10 μL of the CCK-8 reagent was added to each well and left to incubate for another 2 h at 37 °C. A microplate spectrophotometer (Infinite M200, TECAN) was used to determine the optical density at 450 nm.

The percentage cell viability at different concentration with respect to control (untreated cells) was calculated by using following equation:

$$\%\ Cell\ viability = \frac{ODtest}{ODcontrol} \times 100$$

2.6.3. Evaluation of PHL/SBE-β-CD-IC effect on caspase 3/7 activation

To evaluate the apoptotic properties, apoptosis mediator (caspase3/7) activity was assessed using caspase-3/7 assay kit (CellEvent™ Caspase-3/7 Green Detection Reagent, Invitrogen by Thermo Fisher Scientific). The experiment was carried out as per the manufacturer's protocol. In brief, the MiaPaCa–2 and A549 cells were exposed to various concentrations of PHL or PHL/SBE-β-CD-IC for 24 h. Caspase reagent was diluted with 2 mL PBS (1:400 ratio) and 5 μL of the diluted reagent was added in each well followed by incubation for 30 min at 37 °C. Finally, GFP fluorescence emitted by the cells was measured using an automated cell counter (Countess™ 3FL, Invitrogen, Thermo Fisher Scientific, Singapore) (λex = 502 nm, λem = 530 nm).

2.6.4. Estimation of reactive oxygen species (ROS) generation

The impact of ROS generation by PHL/SBE-β-CD-IC was assessed using fluorogenic cell permeant 2′,7′-dichlorofluorescein diacetate (DCF-DA) dye. The cells were seeded in 12-well microplates and cultured overnight at 37 °C for the experiment. Following that, the cells were treated for 24 h with varying concentrations of PHL and PHL/ SBE-β-CD-IC. After washing with PBS, the cells were exposed to 20 μM DCF-DA and incubated for 30 min at 37 °C [26]. After the PBS wash, the fluorescence intensity was recorded using microplate spectrophotometer (Synergy-H1, hybrid reader, BioTek®) and images were captured at 20x magnification at Ex-488 nm and Em-535 nm using confocal microscope (DMi8 S, Leica Stellaris 5, Illinois, USA).

2.6.5. Mitochondrial membrane potential (MMP) analysis

To evaluate the effect of PHL/SBE-β-CD-IC on the mitochondrial membrane potential, JC – 1 (Tetraethylbenzimidazolylcarbocyanine iodide, mitochondrial membrane potential probe, Invitrogen by Thermo Fisher Scientific) staining was carried out [27]. In brief, MiaPaCa–2 and A549 cells were seeded for 24 h and after adherence; the cells were treated with various concentrations of PHL and PHL/SBE-β-CD-IC for 24 h. After treatment, cells were washed with PBS followed by incubation with JC-1 dye (2 μM) for 20 min in dark at 37 °C. At last, the final wash was given to remove the dye from the cells. The imaging was performed using confocal microscope (Leica Stellaris 5, Illinois, USA) at 20x magnification and quantification of change in flourorscence intensity was performed using ImageJ software (version,1.53e).

2.7. Statistical analysis

Each experiment was conducted in triplicates and findings were presented as mean ± standard deviation. The one-way analysis of variance (ANOVA) and Tukey's post hoc test was utilized as statistical significance test using the GraphPad Prism 9 programme (GraphPad Software Inc, CA, USA). The values having $P < 0.05$ were considered significant between PHL and PHL/SBE-β-CD-IC.

3. Results and discussion

3.1. Determination of apparent stability constant (Ks) and molar stoichiometry

Phase solubility studies of PHL were carried out as an initial screening procedure to ascertain the apparent binding potential and solubilizing capabilities of modified cyclodextrin derivatives **[Supplementary Fig. S1]**. The phase solubility curves of PHL with (2-HP)-β-CD, M-β-CD and SBE-β-CD represented linear plot (A_L-type curves) **[Fig. 2 (a)]** and concentration dependent association with CDs indicating 1:1 M stoichiometric relation between the host and guest molecules as per Higuchi and Connor **[Supplementary Fig. S2]** [28].

The (2-HP)-β-CD and M-β-CD derivatives demonstrated apparent stability constant values 11,452 M^{-1} and 14,676 M^{-1}, respectively. However, higher apparent stability constant value (15,856 M^{-1}) was obtained in case of SBE-β-CD derivative. A higher stability constant (Ks) value usually denotes improved inclusion effects in terms of better binding and solubilization capability, moreover, the values obtained are in accordance with the already published reports [19,28–30] **[Supplementary Table S1]**. Additionally, aqueous solutions of (2-HP)-β-CD and M-β-CD at 20 mM concentration resulted in ~ 138 folds and ~ 161 folds increment in PHL aqueous solubility as compared to free PHL (without CDs), respectively. In contrast, SBE-β-CD displayed ~ 177 folds increment in PHL solubility at 20 mM concentration **[Fig. 2(b)]**.

The higher apparent stability constant and enhanced solubilizing capability of SBE-β-CD for PHL may be attributed to presence of multiple negative charges due to sulfobutyl moieties in aqueous solution. Moreover, the repulsion between these negatively charged substituents at the SBE-β-CD portals effectively extend/expands the hydrophobic cavity space of the CD molecule providing ample space for inclusion of PHL [14,31]. Higher apparent stability constant and solubilizing power of SBE-β-CD towards PHL in contrast to other two modified β-CD derivatives [(2-HP)-β-CD and M-β-CD] justifies its superiority over other CD derivatives. Therefore, SBE-β-CD was selected as ideal carrier for PHL inclusion complex formation.

3.2. Characterizations of PHL/SBE-β-CD inclusion complex (IC)

3.2.1. Determination of embedding and loading efficiency

The embedding efficiency directly represents the capability of cyclodextrin to encapsulate the guest molecule. The PHL/SBE-β-CD-IC displayed embedding efficiency of ~ 69.13 ± 0.93 %, indicating

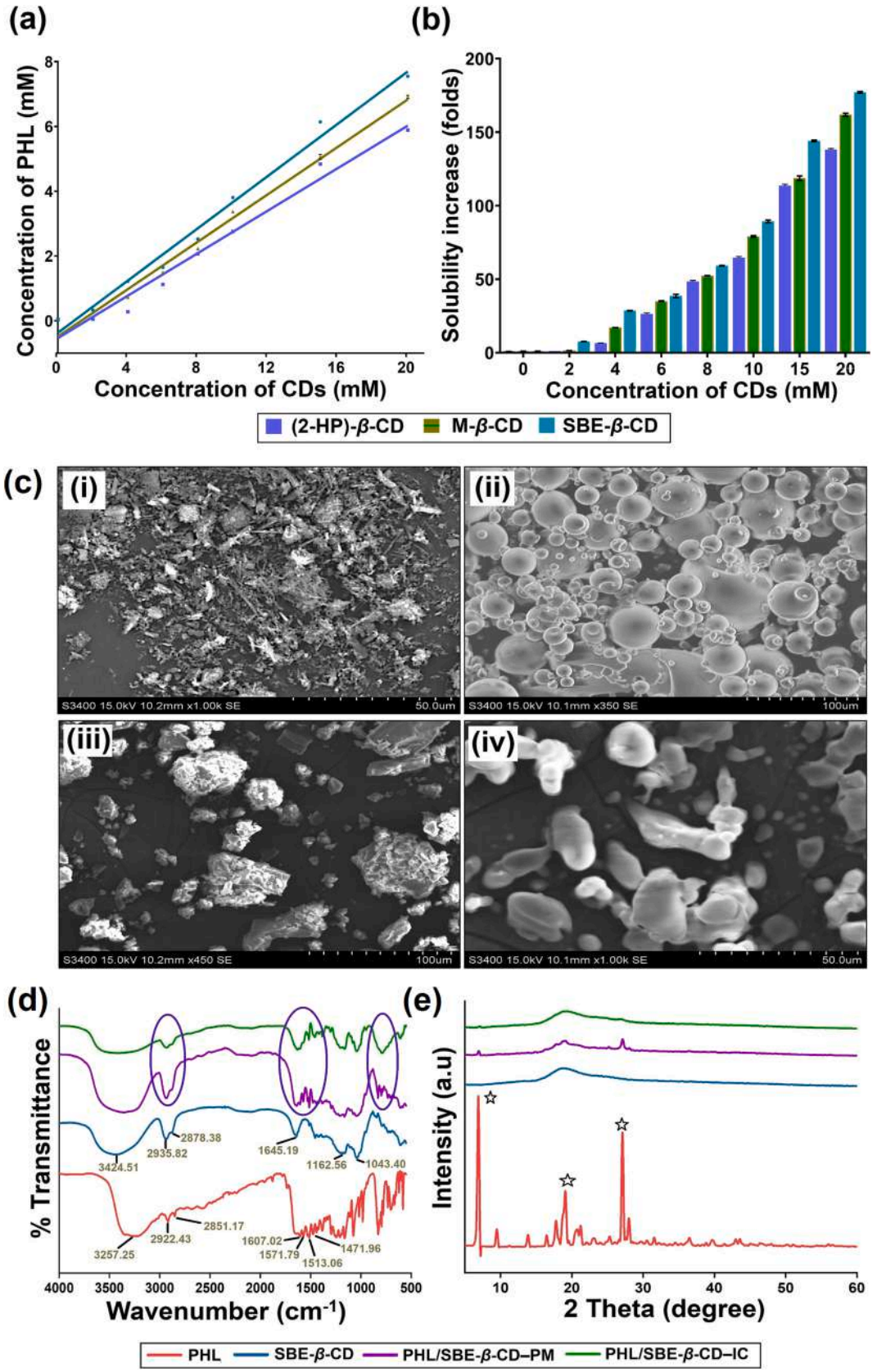

Fig. 2. Graphical representation of (a) Phase solubility curve of phloretin (PHL) at increasing concentrations of β-cyclodextrin derivatives (0–20 mM); (b) Folds increment in aqueous solubility of PHL in the presence of cyclodextrin (n = 3) (c) Scanning electron microscopy of (i) PHL, (ii) SBE-β-CD, (iii) PHL/SBE-β-CD-IC and (iv) corresponding physical mixtures; (d) Stacked FT-IR spectra and (e) PXRD diffractograms of PHL, SBE-β-CD, PHL/SBE-β-CD-IC and corresponding physical mixtures. In FT-IR spectra, oval marking indicates shifted, decreased, and concealed prominent absorption peaks and bands of PHL after formation of inclusion complex. In XRD diffractograms of PHL, star indicates its intensive sharp crystalline peaks at 2θ degree: 6.94°, 19.1° and 27.12°.

significant potential of SBE-β-CD to encapsulate the PHL. The loading content was observed to be 8.57 ± 0.12 % revealing exceptional quality of prepared IC to load the PHL molecule [23].

3.2.2. Surface morphological analysis

The SEM images of native PHL displayed rod like crystal structures, whereas, SBE-β-CD displayed smooth spherical shape with cavity size variability and cavity fragments. The surface morphology of PM displayed distorted spherical particles of SBE-β-CD with PHL particles clung over its surface [2,32]. On the contrary, the microphotograph of freeze-dried IC of PHL demonstrated smooth surfaces and complete disappearance of distinctive rod like crystals of PHL [33] **[**Fig. 2**(c)]**. It may be concluded that due to the possible interaction between host and guest molecules, the innate morphologies of the native components (PHL and SBE-β-CD) was altered in case of PHL/SBE-β-CD-IC [34,35]. The surface morphological changes in case of IC revealed successful formation of new solid phases, efficient incorporation of PHL inside CD cavity and effectiveness of the lyophilization mechanism.

3.2.3. Fourier transform infrared spectroscopy (FT-IR)

The FT-IR spectrum of PHL demonstrated a strong and broad absorption band ranging from 3351.11 cm^{-1} to 3189.62 cm^{-1} due to —OH stretching vibrations **[**Fig. 2**(d)]**. The stretching vibration of C═C bonds of aromatic ring in PHL resulted in prominent absorption bands at 1607.02 cm^{-1},1571.79 cm^{-1}, 1513.06 cm^{-1} and 1471.96 cm^{-1}. The absorption bands at 2922.43 cm^{-1} and 1636.38 cm^{-1} were attributed to the asymmetrical stretching vibration of —CH_2 and C═O groups, respectively [2,19]. The FT-IR spectrum of SBE-β-CD presented a broad band from 3762.23 cm^{-1} to 3104.47 cm^{-1} owing to O—H stretching vibrations. Moreover, C—H stretching bands were observed at 2935.82 cm^{-1} and 2878.38 cm^{-1}. Due to H—O—H bending of water molecules present in the portals of SBE-β-CD, a prominent band at 1645.19 cm^{-1} was also observed. The stretching vibrations of —CH and O═S═O group demonstrated absorption bands at 1162.56 cm^{-1} and 1043.40 cm^{-1}, respectively [32].

The spectrum of PM was just the superimposition of host and guest molecules without showing any obvious difference. However, in IC, broad absorption band attributed to the hydroxyl group stretching and asymmetrical stretching vibration of –CH_2 groups undergoes comparative changes in terms of intensity and width as compared to PM and pure molecules, indicating that PHL may partly embedded inside the hollow portal of the SBE-β-CD. Moreover, FT-IR spectra of IC demonstrated masking, shifting, and decreased intensity of absorption bands/peaks of PHL after IC formation [28]. The obvious discrepancies between the FT-IR spectra of the free and complex forms of PHL provide evidences of possible interactions between PHL and SBE-β-CD. However, additional characterizations were carried out to validate the formation of PHL/SBE-β-CD-IC.

3.2.4. Powder X-ray diffractometry (PXRD)

The diffractogram of PHL displayed typical sharp peaks at 6.94°, 19.1° and 27.12° and several minor peaks on 2θ scale, due to its native crystalline state **[**Fig. 2**(e)]** [36,37]. Contrarily, the diffractogram of the SBE-β-CD did not exhibit any prominent peaks; instead, only a hollow pattern was observed. The diffractogram of PM was mare a summation of the individual diffractograms, with small and less intense peaks of PHL at 6.94° and 27.12°. In contrast, PXRD pattern of IC displayed amorphous hollow pattern similar to SBE-β-CD diffractogram with comprehensive concealing of crystalline peaks of PHL. It may be inferred that during lyophilization process the PHL molecule get encapsulated inside SBE-β-CD cavity and thereby preventing molecular aggregation of PHL [28,31,32]. XRD patterns served as unambiguous evidence of transformation of self-lattice arrangement of PHL from native crystalline state to amorphous state after its inclusion with SBE-β-CD.

3.2.5. Proton nuclear magnetic resonance (^{1}H NMR) and two–dimensional nuclear overhauser effect spectroscopy (2D – NMR)

NMR spectroscopy has been employed as a reliable method for analyzing the supramolecular interaction between host–guest assembly [33]. These interactions cause small chemical shift differences (Δδ) in NMR spectrum due to altered chemical and electronic environments [38]. To gain molecular level insight into the inclusion mode of the PHL inside the SBE-β-CD cavity, ^{1}H NMR spectroscopic studies of PHL, SBE-β-CD, and PHL/SBE-β-CD-IC was carried out.

The ^{1}H NMR spectra of PHL depict peaks δ_H at ~12.18 ppm, ~12.18 ppm, 10.28 ppm and ~9.07 ppm that are associated with protons of hydroxyl group of H-6′-OH (s), H-2′-OH (s), H-4′-OH (s) and H-4-OH (s), respectively. In addition, peaks at 7.02 ppm, 6.67 ppm, 5.81 ppm, 3.22 ppm and 2.78 ppm were observed due to H-2,6 (d), H-3,5 (d), H-3′,5′ (s), H-β (m) and H-α (m), respectively [39]. The chemical shifts of SBE-β-CD lies in the range of 1.5 δ – 5.3 ppm, which agreed with already published report [34]. More specifically, H-1, H-2, H-3, H-4, H-5 and H-6 protons demonstrated chemical shifts at δ_H value of 5.24 ppm, 3.62 ppm, 5.11 ppm, 3.50 ppm, 3.89 ppm and 3.73 ppm, respectively. Moreover, the protons of sulfobutyl ether moiety demonstrated chemical shift at δ value of 2.96 and 1.80 ppm [33].

The proton NMR spectra of PHL in the native and complex state were examined for better molecular interaction insight. Despite PHL's extremely poor aqueous solubility, all of the predicted aromatic protons of PHL were clearly detectable in NMR spectrum of PHL/SBE-β-CD-IC in D_2O providing conclusive proof of inclusion of PHL. Similar findings were observed in the case of other inclusion complexes with flavonoids such as genistein and 2R,3R – dihydromyricetin [28,40]. Moreover, protons NMR spectra of PHL in complexed state (in D_2O) exhibited significant downfield shifts **[**Fig. 3 **(a)]**. It can be clearly seen in PHL/SBE-β-CD-IC spectra that H-2,6 and H-3,5 protons of aromatic phenyl ring of PHL demonstrated significant downfield shifting (Δδ) of −0.053 ppm and −0.149 ppm, respectively [change in chemical shift were calculated from equation ($\Delta\delta = \delta_{complex} - \delta_{free\ PHL}$)]. Additionally, it is important to note that complexed state NMR spectra do not display the proton signals of the H-α and H-β protons of PHL because they are difficult to analyze due to substantial overlapping of protons associated with sulfobutyl chains of the SBE-β-CD **[Supplementary Table S2]**.

To decipher the mode of orientation of PHL inside the SBE-β-CD cavity, we further carried out 2D-NOESY analysis. Typically, it was found that CD protons lying at the inner cavity (H-3 and H-5) experiences an increase in electron density after the IC formation , whereas, CD protons lying on the corona (H-1, H-2, and H-4) are not significantly affected or only experienced a marginal shift upon complexation because they are not directly involved in molecular interactions [35]. The 2D-NOESY spectra of IC in D_2O demonstrated key correlation between the H-5 protons of CD with the aromatic doublets [H-2,6 (7.026 ppm) and H-3,5 (6.672 ppm)] of the hydroxyphenyl moiety (ring-A) of PHL. These correlations cause slight downward chemical shift of aromatic ring protons H-2,6 (Δδ: 0.053) and H-3,5 (Δδ: 0.149). In addition, H-3 proton of SBE-β-CD also demonstrated molecular interaction with H-α and H-β protons of PHL. These interaction causes significant shifting of protons present in the inner portal of SBE-β-CD [H-5 protons (Δδ): −0.076 ppm, H-3 proton (Δδ): −0.041] **[**Fig. 3**(b)]**. The upfield chemical shift of H-5 protons might be attributed to its involvement in hydrogen bonding. While upfield shifting of H-3 protons might be attributable to the dense electron cloud experienced by H-3 proton as a result of the nearby C═O group [34,41].

Thus, it can be inferred from these significant key correlations that the aromatic hydroxyphenyl ring (ring A) of PHL was inserted in SBE-β-CD cavity from the wider side of the rim **[**Fig. 3**(c)]**. The findings of NMR analysis demonstrated the successful IC formation which corroborates with the evidence observed from solid state characterizations such as FT-IR, PXRD and DSC.

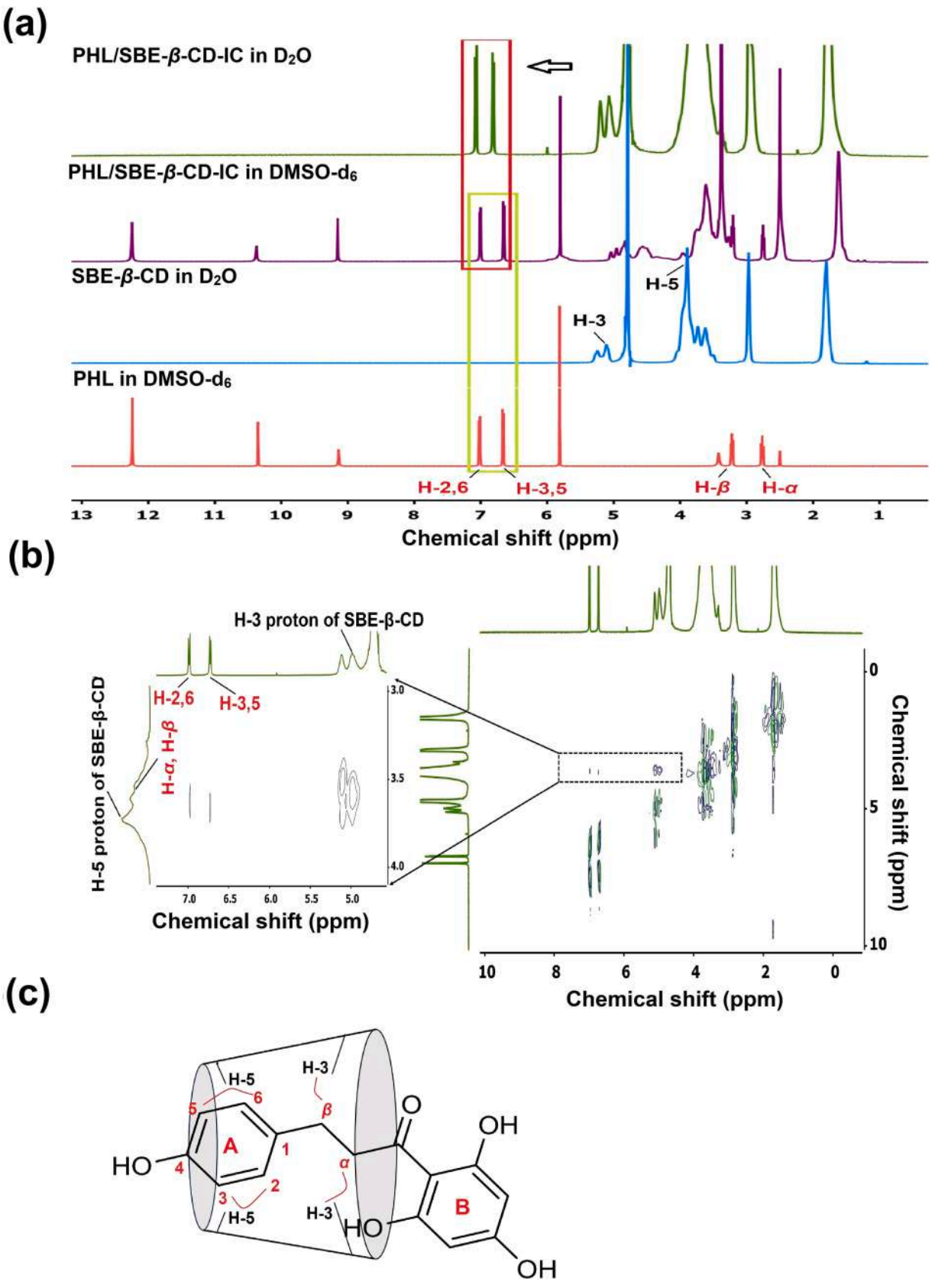

Fig. 3. Unveiling the PHLmode of orientation inside the SBE-*β*-CD portal *via* nuclear magnetic resonance spectroscopy (a) ^{1}H NMR of PHL (in DMSO-d_6), SBE-*β*-CD (in D_2O) and PHL/SBE-*β*-CD-IC (in DMSO-d_6 and D_2O); (b) 2D-NOESY spectra of PHL/SBE-*β*-CD-IC in D_2O. The chemical shift at 4.79 ppm and 2.50 ppm was observed due to D_2O and DMSO-d_6, respectively. (c) Schematic representation of mode of orientation of PHL inside SBE-*β*-CD cavity demonstrating protons of PHL interacting with protons lying in the inner cavity of cyclodextrin.

3.2.6. Differential scanning calorimetry (DSC) analysis

The DSC curve of PHL demonstrated a sharp endothermic peak at 269.12 °C, implying the melting point (T_m) of PHL, which correlates with the already published reports **[**Fig. 4**(a)]** [9,37]. DSC thermogram of SBE-*β*-CD represented a broad and sharp endothermic peak at 258.21 °C attributed to the dehydration and decomposition of SBE-*β*-CD [42]. In the thermogram of PM, a broad peak was observed which might be due to loss of water molecules from CD. In addition, a less intense peak (near melting point of PHL) was also observed indicating presence of free PHL crystals in PM [17]. Conversely, in IC thermogram, the endothermic peak of PHL melting at 269.12 °C was completely vanished, indicating apparent inclusion of PHL in SBE-*β*-CD cavity.

3.2.7. Thermal gravimetric analysis (TGA)

The degradation behavior of PHL, SBE-*β*-CD-IC and PM were characterized by TGA curves **[**Fig. 4**(b)]**. The PHL displayed a single step decomposition that began at about 250.10 °C and reached its maximum decomposition rate at about 350.83 °C. At 700 °C, about 35 % of the original sample was still present as a charred residue [43]. The thermal heating of SBE-*β*-CD showed two distinct phases of weight loss due to dehydration (water loss, 30 to 115 °C) and degradation (267 °C to 430 °C) [44]. TGA pattern of PM and IC demonstrated multiple step weight loss; dehydration of water embedded in CD cavity, and deterioration of PHL and SBE-*β*-CD, respectively. Although, it should be notable that, the weight loss attributed to the dehydration of water molecules embedded in CD cavity (i.e., first stage of weight loss) is relatively lower in case of IC (6.17 %) as compared to PM (9.01 %) and SBE-*β*-CD (11.09 %). The relatively low weight loss at the first stage in case of IC was due to replacement and release of water molecules from the hydrophobic cavity of SBE-*β*-CD by PHL during incubation period and lyophilization process [31,32].

In particular, it was found that the thermal degradation of PHL in PHL/SBE-*β*-CD was pushed to a little higher temperature, from 250.10° to 275.31 °C, in both the TGA curves and the derivative DTG graph **[**Fig. 4**(c)]**.

3.2.8. In vitro dissolution study

The *in vitro* dissolution profile of PHL demonstrated ~ 42 % dissolution after 120 min. In contrast, freeze dried IC of PHL demonstrated ~ 65 % of PHL dissolution after similar time point **[**Fig. 4**(d)]**. The ~ 1.5-folds increment in dissolution profile of PHL from inclusion complex was due to solubilization effect of SBE-*β*-CD, transformation of PHL crystalline phase to more soluble amorphous state (as evident from SEM, PXRD and DSC studies) and formation of non-covalent interactions (including hydrogen bonding, van der Waals, electrostatic and hydrophobic interactions) between the host and guest molecules [24].

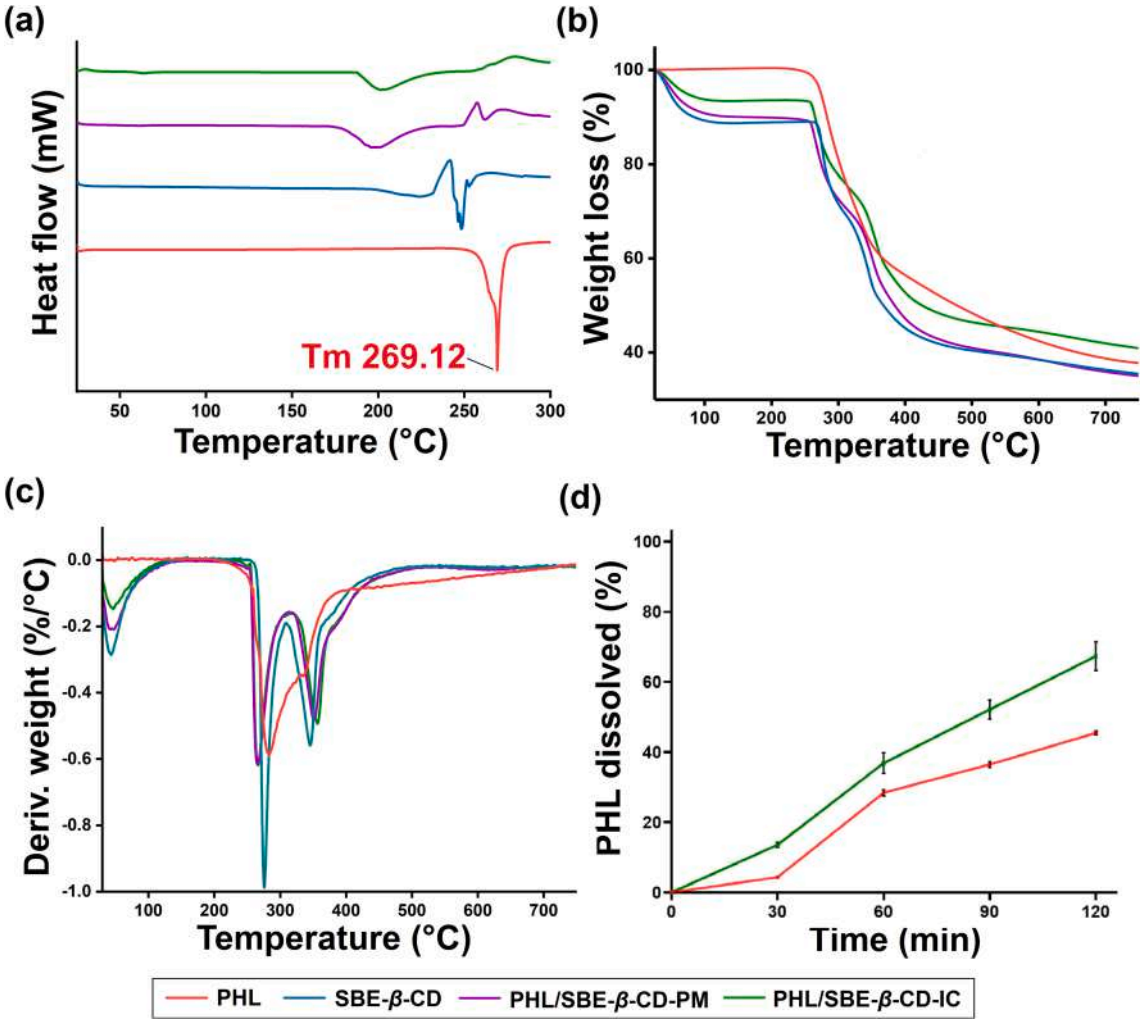

Fig. 4. Thermal behavior analysis and *in vitro* dissolution profile of inclusion complex (a) DSC thermograms, (b) TGA thermograms and (c) DTA thermograms of PHL, SBE-*β*-CD, PHL/SBE-*β*-CD-IC and physical mixture (d) *In vitro* dissolution profile of PHL and PHL/SBE-*β*-CD-IC at physiological condition. The results were expressed as the mean values ± SD; n = 3.

3.3. Evaluation of anti-tumor activity of PHL/SBE-β-CD-IC

3.3.1. Effect of PHL/SBE-β-CD-IC on cell viability of MiaPaCa–2 and A549

The cell viability was investigated to evaluate the enhanced *in vitro* antitumor efficacy of PHL/SBE-β-CD-IC in comparison to free PHL. The results revealed that PHL/SBE-β-CD-IC exerts significantly stronger inhibitory effects on both the cancer cell lines when compared to free PHL [45]. More specifically, the PHL demonstrated IC_{50} value of 198.91 ± 6.6 μM, whereas, PHL/SBE-β-CD-IC demonstrated strong inhibitory effect with IC_{50} values of 135.58 ± 6.7 μM in MiaPaCa–2 cells **[**Fig. 5 **(a)] .** Similar results were observed with A549 cells, where PHL exerted relatively weak growth inhibitory effect when compared with PHL/SBE-β-CD-IC with IC_{50} values 172.83 ± 1.4 μM and 111.51 ± 1.6 μM, respectively **[**Fig. 5**(b)] .** The strong inhibitory effects of freeze-dried PHL/SBE-β-CD-IC on both cell lines might be attributed to the higher solubilizing effect provid ed by SBE-β-CD and enhanced cellular internalization/uptake [46–49]. Moreover, it is important to note that SBE-β-CD in its native form has negligible cytotoxic effect even up to 1 mM concentration on both these cell lines (data not shown).

3.3.2. Effect of PHL/SBE-β-CD-IC on caspase 3/7 activation

Apoptosis (programmed cell death) is an inbuilt biological cell death process caused by specific cellular signaling mechanisms. Several diseases including cancer, autoimmune and degenerative conditions may result from anomalies in the regulation of cell death [50]. Caspases (cysteine aspartate-specific proteases) are classified into two categories: initiator caspases [caspase −2, −8, −9, −10, −11, and −12) and effector caspases (caspase −3, −6, and −7). The initiator caspases initiate downstream apoptosis signaling by the proteolytic cleavage of effector caspases for their activation. As a consequence, intracellular proteins are proteolytically degraded by active effector caspases, which leads to programmed cell death.

Thus, to establish the apoptotic procedure generated by the PHL/SBE-β-CD-IC, the effector caspase activity was assessed using the Cell Event™ Caspase-3/7 Green Detection kit [51]. The detection kit reagent is composed of four-amino acid peptide (DEVD) that is conjugated to a nucleic acid – binding dye. In non-apoptotic cells, the reagent is non-fluorescent, however during apoptosis, active caspases 3 and 7 cleave the DEVD peptide, allowing the dye to attach with DNA which triggers a vibrant green fluorogenic response as indicator of apoptosis [52]. The results demonstrated that both PHL and PHL/SBE-β-CD-IC treated cell lines undergo caspase-mediated cell death in a concentration-dependent manner. The cells treated with native PHL at 200 μM concentration demonstrated 46.01 ± 4.58 % apoptosis inducing potential in MiaPaCa-2 cells and 35.66 ± 2.08 % in A549 cells. However, comparative studies demonstrated that inclusion complex of PHL induce apoptosis more efficiently than native PHL. It was observed that PHL/SBE-β-CD-IC demonstrated higher caspase-dependent apoptosis induction (73.66 ± 1.17 %) in both MiaPaCa–2 cells **[**Fig. 5**(c)]** and A549 cells (59.01 ± 2.64 %) at highest studied PHL concentration (200 μM) **[**Fig. 5**(d)] .** Therefore, it could be postulated that PHL/SBE-β-CD-

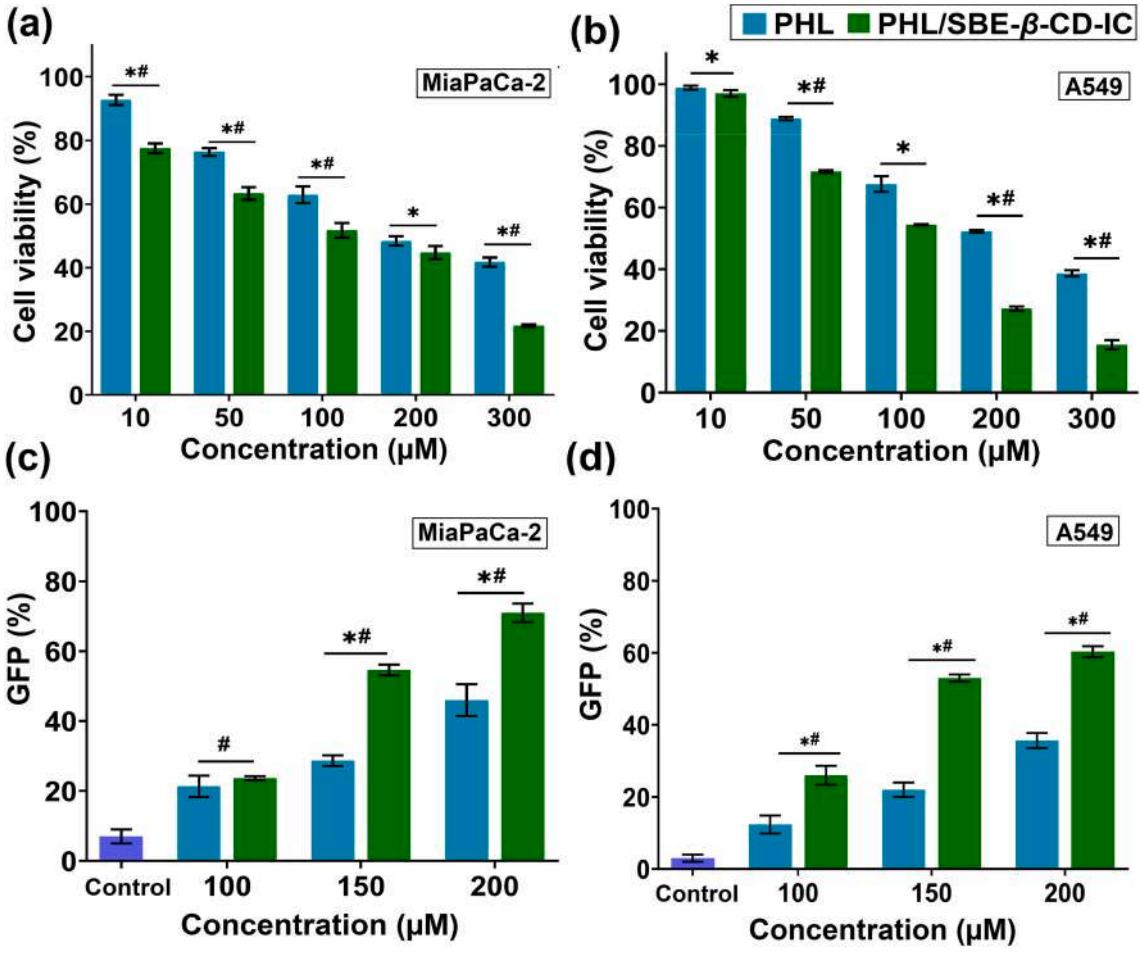

Fig. 5. Dose dependent cytotoxic effect of PHL and PHL/SBE-β-CD-IC assessed on cancer cell lines upon 24 h treatment. Cell viability graph upon treatment of PHL and PHL/SBE-β-CD-IC in (a) MiaPaCa-2 and (b) A549 cell lines. Caspase 3/7 analysis on (c) MiaPaCa-2 and (d) A549 cells to assess the apoptotic activity of inclusion complex after 24 h treatment. Data presented as mean ± SD, n = 3. *p < 0.05 represent significant difference between the mean of all groups with respect to control. # p < 0.05 represent significant difference between the mean of PHL concentration with respective inclusion complex concentrations.

IC triggers cell apoptosis by activating caspase 3/7 apoptotic pathway and might be the possible mechanism behind anti-proliferative activity of the complex.

3.3.3. Reactive oxygen species (ROS) generation by PHL/SBE-β-CD-IC

ROS plays crucial role in cell signaling and regulation of apoptotic signaling pathways mediated by death receptors, mitochondria, and endoplasmic reticulum [53]. The results demonstrated that both PHL and its inclusion complex follow concentration-dependent accumulation of ROS in both the cell lines. The cells treated with native PHL at highest tested concentration (200 μM) cause 98.33 % and 120.37 % ROS production in MiaPaCa-2 and A549 cells, respectively. Whereas, MiaPaCa-2 cells treated with PHL/SBE-β-CD-IC demonstrated 37.65 %, 79.77 % and 123.73 % increase in ROS generation. Likewise, A549 cells treated with PHL/SBE-β-CD-IC demonstrated 55.83 %, 129.61 % and 192.20 % higher ROS production at PHL concentrations 100, 150 and 200 μM, respectively, when compared with the untreated cells (control) **[**Fig. 6**]**. The enhanced green fluorescence intensity on treatment with higher concentration of PHL and IC demonstrated high intracellular ROS generation [5]. The variation in ROS production observed on both cell lines might be due to the difference in the origin, molecular mechanism and metabolic pathways of these cell lines [54].

3.3.4. PHL/SBE-β-CD-IC induced MMP depolarization

The disruption of MMP is associated with the intrinsic apoptotic pathway. Cancer cells progressing towards apoptosis contain j monomers that generate green fluorescence, while healthy cells with healthy mitochondria contain j aggregates emitting red fluorescence. Increased mitochondrial permeability and changes in mitochondrial membrane potential is usually observed by alterations in the fluorescence intensity of JC-1 ratio of j aggregates to j monomer. Therefore, JC-1 dye staining experiment was used to assess the impact of IC on the mitochondrial membrane potential [27]. Our results clearly demonstrated that treatment of PHL/SBE-β-CD-IC provoked significantly higher depolarization in mitochondrial membrane potential when compared to free PHL as the ratio of j aggregates to j-monomers was significantly decreased in both A549 and MiaPaCa–2 cells after inclusion complex treatment **[**Fig. 7**]**. In addition, treatment of PHL/SBE-β-CD-IC (equivalent to 200 μM PHL) results in ~ 11 folds and ~ 7 folds reduction in the j aggregate/j monomer ratio in MiaPaCa-2 and A549 cells respectively**.** The reduction in j aggregate/j monomer ratio by inclusion complex indicates its anti-proliferative effects via intrinsic apoptotic pathway associated with disturbance in MMP.

4. Conclusion

In the present study, we investigated the solubilizing ability of different derivatives of β-CDs with PHL and found that SBE-β-CD exhibits highest solubilizing ability towards PHL. Therefore, we developed PHL/SBE-β-CD inclusion complex by lyophilization process. The experiments and characterization method conducted in this study clearly authenticated the application of SBE-β-CD as a better choice to enhance the aqueous solubility of PHL. Solid state characterizations (FT-IR, DSC, TGA, PXRD, and SEM) presented strong evidence of inclusion of the PHL inside CD cavity. Furthermore, ^{1}H NMR and 2D-NOESY analysis indicated the insertion of aromatic hydroxyphenyl ring (ring A) of PHL

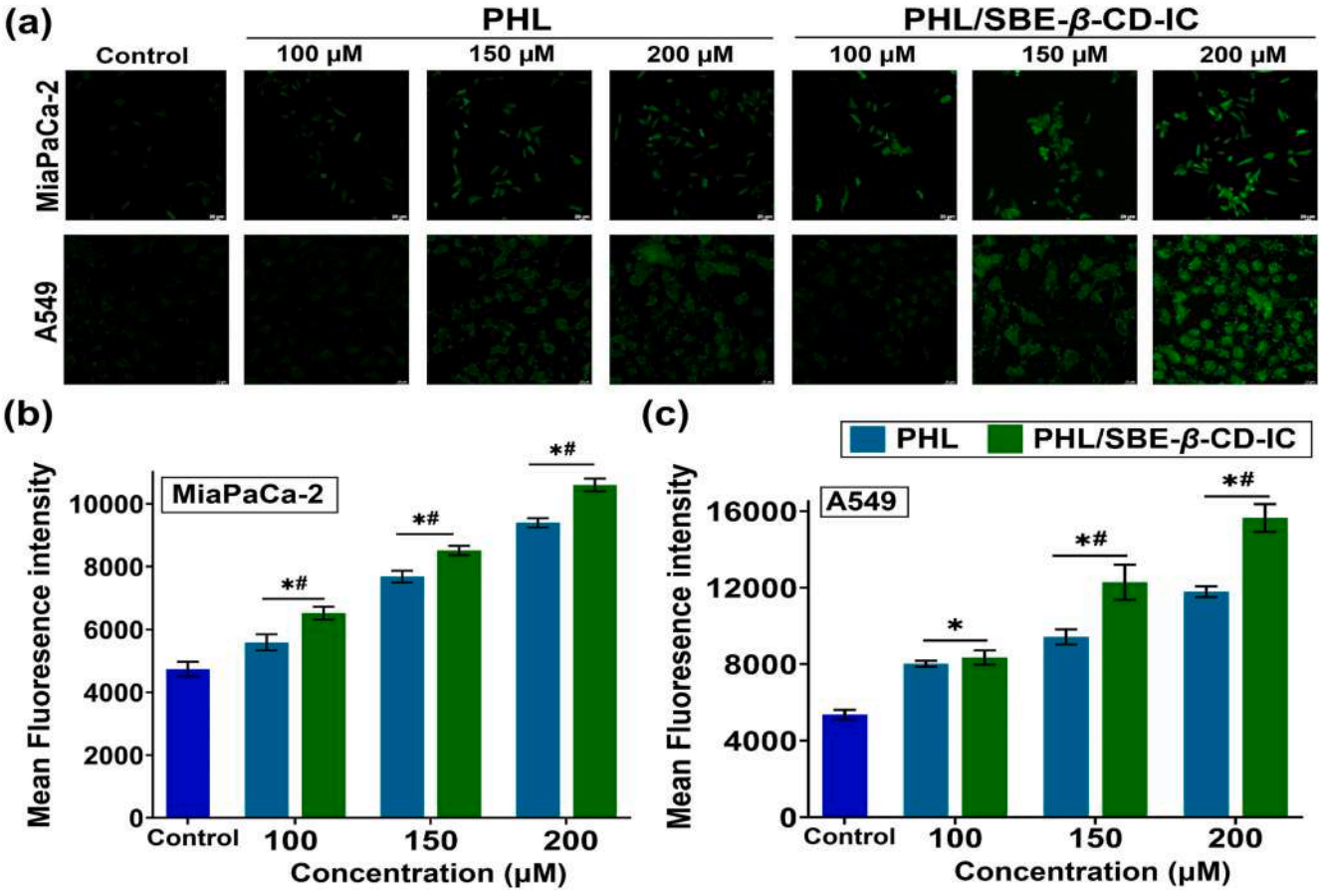

Fig. 6. Reactive oxygen species (ROS) accumulation after treatment with various concentration of PHL and PHL/SBE-β-CD-IC in MiaPaCa-2 and A549 cells (a) Microscopy images of detection of intracellular ROS generation in MiaPaCa–2 and A549 cells; Quantitative analysis of accumulation of ROS in (b) MiaPaCa-2 and (c) A549 cells respectively. Data presented as mean ± SD, n = 3. *p < 0.05 represent significant difference between the mean of all groups with respect to control. # p < 0.05 represent significant difference between the mean of PHL concentration with respective inclusion complex concentrations.

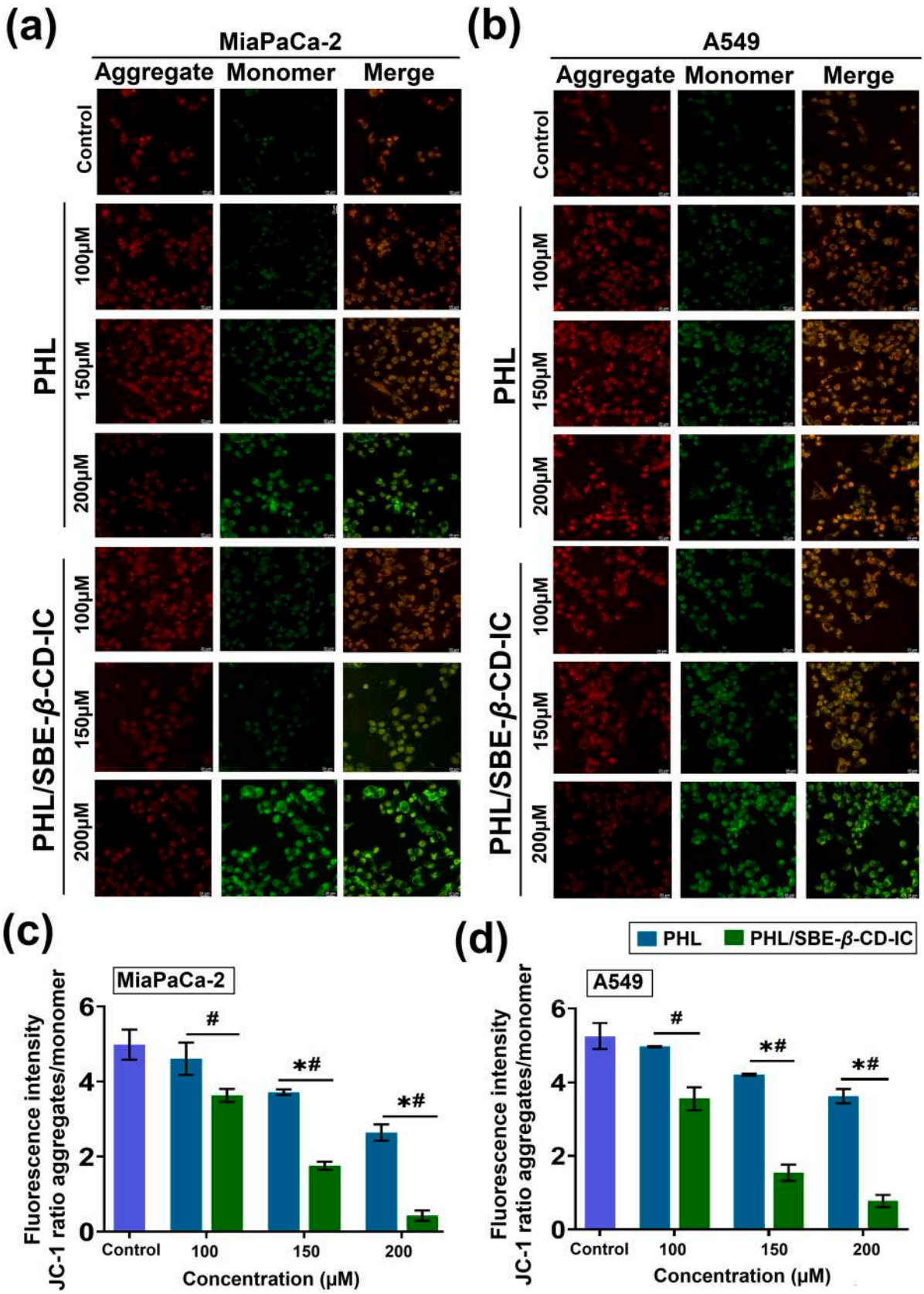

Fig. 7. Determination of mitochondrial membrane potential of (a) MiaPaCa-2 and (b) A549 cells after treatment of phloretin and PHL/SBE-β-CD-IC via JC-1 staining; The quantification of change in fluorescence intensity of JC-1 dye was performed using ImageJ software (version1.53e) in (c) MiaPaCa-2 and (d) A549 cells. The reduction in j aggregate/j monomer ratio by inclusion complex indicates its antiproliferative effects via intrinsic apoptotic pathway associated with disturbance in MMP. Data represented mean $\pm$ SD, n = 3. *$p < 0.05$ represents significant difference between the mean of all groups with respect to control. # $p < 0.05$ represents significant difference between the mean of PHL concentration with respective inclusion complex concentrations.

inside the SBE-β-CD cavity, corroborating the evidence collected from solid-state characterizations. *In vitro* dissolution test demonstrated improved dissolution profile of PHL/SBE-β-CD-IC as compared to free PHL.

To investigate the anticancer activity of PHL/SBE-β-CD-IC, cytotoxicity , caspase 3/7 activation assay, ROS generation and disturbance in MMP were evaluated. *In vitro* cytotoxicity assay on MiaPaCa–2 as well as A549 cells demonstrated a higher antiproliferative activity of IC compared to free PHL. In addition, based on *in vitro* cell culture assays, it can be concluded that PHL/SBE-β-CD-IC induces apoptosis *via* activation of caspase 3/7, generation of reactive oxygen species and depolarization of mitochondrial membrane potential in both the cell lines (MiaPaCa–2 and A549). In nutshell, our findings demonstrated that the ICs formed with SBE-β-CD can be a promising approach for the delivery of phloretin and it could be effectively applied to other hydrophobic bioactive molecules for expanding their application in the food sector.

CRediT authorship contribution statement

Nabab Khan: Writing – original draft, Methodology, Formal analysis. **Garima Slathia:** Writing – original draft, Methodology, Formal analysis. **Ankit Saneja:** Writing – review & editing, Supervision, Project administration, Funding acquisition, Conceptualization.

Declaration of competing interest

The authors declare that they have no known competing financial interests or personal relationships that could have appeared to influence the work reported in this paper.

Data availability

Data will be made available on request.

Acknowledgements

The authors are grateful to the Director, CSIR-IHBT, Palampur for his continuous support and encouragement. A.S acknowledges financial assistance from ICMR, New Delhi (file number: 5/9/1423/2022-Nut) and CSIR (MLP 204). N.K acknowledges Council of Scientific and Industrial Research (CSIR), New Delhi, for providing Junior Research fellowship (File GATE31/0054(12027)/2021-EMR-I). G.S. acknowledges Indian Council of Medical Research (ICMR), New Delhi, for providing project Junior research fellowship. The Authors acknowledge the Advanced Materials Research Center, Indian Institute of Technology, Mandi for carrying out PXRD analyses. CSIR—Indian Institute of Integrative Medicine, Jammu, CSIR—Institute of Microbial Technology, Chandigarh and National Institute of Pharmaceutical Education and Research, Hyderabad for performing FT-IR, TGA and NMR analyses, respectively. Figure 1 is drawn from the material provided by Servier Medical Art (www.smart.servier.com) under the Creative Commons Attribution 3.0 Unported License.The manuscript bears institutional communication number 5418.

Appendix A. Supplementary material

Supplementary data to this article can be found online at https://doi.org/10.1016/j.molliq.2023.123348.

References

[1] Y. Wang, D. Li, H. Lin, S. Jiang, L. Han, S. Hou, S. Lin, Z. Cheng, W. Bian, X. Zhang, Food Sci. Nutr. 8 (2020) 3545.
[2] J. Chhimwal, R.K. Dhritlahre, P. Anand, V. Patial, A. Saneja, Y.S. Padwad, Biomater. Adv. (2023), 213627.
[3] S. Behzad, A. Sureda, D. Barreca, S.F. Nabavi, L. Rastrelli, S.M. Nabavi, Phytochem. Rev. 16 (2017) 527.
[4] L. Wang, Z.W. Li, W. Zhang, R. Xu, F. Gao, Y.F. Liu, Y.J. Li, Molecules (Basel, Switzerland) 19 (2014) 16447.
[5] H.S. Tuli, P. Rath, A. Chauhan, S. Ramniwas, K. Vashishth, M. Varol, V. Jaswal, S. Haque, K. Sak, Molecules (Basel, Switzerland) 27 (2022) 8819.
[6] L. Gu, R. Sun, W. Wang, Q.J.C. Xia, Lipids 242 (2022), 105150.
[7] F. Wang, X. Xiao, Y. Yuan, J. Liu, Y. Liu, F.C. Yi, Food Chem. 308 (2020), 125569.
[8] A.V.A. Mariadoss, K. Saravanakumar, A. Sathiyaseelan, V. Karthikkumar, M. H. Wang, Int. J. Biol. Macromol. 130 (2019) 997.
[9] S. Nam, S.Y. Lee, H.J. Cho, J. Colloid Interface Sci. 508 (2017) 112.
[10] J.L. Gonzalez-Alfonso, Z. Ubiparip, E. Jimenez-Ortega, A. Poveda, C. Alonso, L. Coderch, J. Jimenez-Barbero, J. Sanz-Aparicio, A.O. Ballesteros, T. Desmet, F. J. Plou, Adv. Synth. Catal. 363 (2021) 3079.
[11] A. Cid-Samamed, J. Rakmai, J.C. Mejuto, J. Simal-Gandara, G.J.F.C. Astray, Food Chem. 384 (2022), 132467.
[12] A.S. Jain, A.A. Date, R.R. Pissurlenkar, E.C. Coutinho, M.S. Nagarsenker, AAPS PharmSciTech 12 (2011) 1163.
[13] X. Xi, J. Huang, S. Zhang, Q. Lu, Z. Fang, C. Li, Q. Zhang, Y. Liu, H. Chen, A. Liu, S. Liu, C. Wang, S. Li, B. Hu, Food Chem. 423 (2023), 136316.
[14] C.V. Pardeshi, R.V. Kothawade, A.R. Markad, S.R. Pardeshi, A.D. Kulkarni, P. J. Chaudhari, M.R. Longhi, N. Dhas, J.B. Naik, S.J. Surana, Carbohydr. Polym. (2022), 120347.
[15] J. Xu, Y. Zhang, X. Li, Y. Zheng, J. Mol. Struct. 1141 (2017) 328.
[16] V.J. Stella, R.A. Rajewski, Int. J. Pharm. 583 (2020), 119396.
[17] L. Ren, Y. Zhou, P. Wei, M. Li, G. Chen, AAPS PharmSciTech 15 (2014) 121.
[18] L. Ferreira, J. Campos, F. Veiga, C. Cardoso, A.C. Paiva-Santos, Eur. J. Pharm. Biopharmaceutics (2022).
[19] Y. Wei, J. Zhang, A.H. Memon, H. Liang, J. Mol. Liq. 236 (2017) 68.
[20] K.A.C.T. Higuchi, Adv. Analytical Chem. Instrumentation 04 (1965) 117.
[21] Q. Zhou, L. Zhong, X. Wei, W. Dou, G. Chou, Z. Wang, Int. J. Pharm. 454 (2013) 125.
[22] S. Gao, C. Bie, Q. Ji, H. Ling, C. Li, Y. Fu, L. Zhao, F. Ye, RSC Adv. 9 (2019) 26109.
[23] P. Han, Y. Zhong, N. An, S. Lu, Q. Wang, J. Dong, J. Mol. Liq. 339 (2021), 116790.
[24] A. Pal, S. Roy, A. Kumar, S. Mahmood, N. Khodapanah, S. Thomas, C. Agatemor, K. Ghosal, ACS Omega 5 (2020) 19968.
[25] Z. Wang, Y. Ma, Y. Jiang, F. Zhou, Y. Wu, H. Jiang, R. Wang, Q. Xu, C. Hua, J. Sci. Food Agr. 102 (2022) 3887.
[26] P. Doan, T. Nguyen, O. Yli-Harja, N.R. Candeias, M. Kandhavelu, Eur. J. Pharm. Sci. 107 (2017) 208.
[27] C. Cottet-Rousselle, X. Ronot, X. Leverve, J.-F. Mayol, Cytometric A 79A (2011) 405.
[28] N. Khan, V. Kumar Bhardwaj, R. Ruchika, A.S. Purohit, J. Mol. Liq. 374 (2023), 121295.
[29] S. Jacob, A.B. Nair, Drug Dev. Res. 79 (2018) 201.
[30] R. Banerjee, H. Chakraborty, M. Sarkar, Biopolymers 75 (2004) 355.
[31] L. Szente, I. Puskás, T. Sohajda, E. Varga, P. Vass, Z.K. Nagy, A. Farkas, B. Várnai, S. Béni, E. Hazai, Carbohydr. Polym. 264 (2021), 118011.
[32] N. Li, B. Feng, Y. Bi, F. Kong, Z. Wang, S. Tan, J. Mol. Struct. (2023), 136686.
[33] D. Xu, X. Li, Y. Huang, Z. Tang, C. Ran, B. Jing, L. Yin, J. Lin, H. Fu, H. Tang, J. Mol. Struct. 1223 (2021), 128969.
[34] A.D. Kulkarni, V.S. Belgamwar, J. Mol. Struct. 1128 (2017) 563.
[35] N. Devasari, C.P. Dora, C. Singh, S.R. Paidi, V. Kumar, M.E. Sobhia, S. Suresh, Carbohydr. Polym. 134 (2015) 547.
[36] S. Mehmood, H. Yu, L. Wang, M.A. Uddin, B.U. Amin, F. Haq, S. Fahad, M. Haroon, Macromol. Res. 30 (2022) 623.
[37] Z. Lu, H. Chen, J. Mo, X. Yuan, D. Wang, X. Zheng, W. Zhu, RSC Adv. 13 (2023) 10914.
[38] Y. Yamamoto, Y. Inoue, J. Carbohydr. Chem. 8 (1989) 29.
[39] P.A. Chacón Morales, C. Santiago Dugarte, J.M. Amaro Luis, Biochem. Syst. Ecol. 77 (2018) 57.
[40] Y. Wu, Y. Xiao, Y. Yue, K. Zhong, Y. Zhao, H. Gao, Food Hydrocoll. 103 (2020), 105718.
[41] Y. Deng, Y. Pang, Y. Guo, Y. Ren, F. Wang, X. Liao, B. Yang, J. Mol. Struct. 1118 (2016) 307.
[42] H.M.H. Soe, S. Chamni, P. Mahalapbutr, N. Kongtaworn, T. Rungrotmongkol, P. Jansook, Carbohydr. Res. 498 (2020), 108190.
[43] X. Hu, Z. Zhou, L. Han, S. Li, W. Zhou, New J. Chem. 44 (2020) 5218.
[44] H. Sadaquat, M. Akhtar, J. Incl. Phenom. Macrocycl. Chem. 96 (2020) 333.
[45] V. Venuti, C. Cannavà, M.C. Cristiano, M. Fresta, D. Majolino, D. Paolino, R. Stancanelli, S. Tommasini, C.A. Ventura, Colloids Surf. B Biointerfaces 115 (2014) 22.
[46] A. Zafar, N.K. Alruwaili, S.S. Imam, O.A. Alsaidan, K.S. Alharbi, E.M. Mostafa, A. Musa, S.J. Gilani, M.M. Ghoneim, S. Alshehri, J. Drug Delivery Sci. Technol. 67 (2022), 102932.
[47] A. Oo, P. Mahalapbutr, K. Krusong, P. Liangsakul, S. Thanasansurapong, V. Reutrakul, C. Kuhakarn, P. Maitarad, A. Silsirivanit, P. Wolschann, J. Mol. Liq. 367 (2022), 120314.
[48] E.E. Eid, A.A. Almaiman, S.A. Alshehade, W. Alsalemi, S. Kamran, F.O. Suliman, M. A. Alshawsh, Molecules (Basel, Switzerland) 28 (2023) 4096.
[49] S. Mohandoss, S. Palanisamy, S. You, J.-J. Shim, Y.R. Lee, J. Mol. Liq. 336 (2021), 116172.
[50] A. Strasser, S. Cory, J.M. Adams, EMBO J. 30 (2011) 3667.
[51] R. Onodera, K. Motoyama, A. Okamatsu, T. Higashi, H. Arima, Sci. Rep. 3 (2013) 1104.

[52] P. Carotenuto, A. Romano, A. Barbato, P. Quadrano, S. Brillante, M. Volpe, L. Ferrante, R. Tammaro, M. Morleo, R.J.C.R. De Cegli, 41, 2022.
[53] M. Redza-Dutordoir, D.A. Averill-Bates, Biochimica et Biophysica Acta (BBA) – Mol. Cell Res. 1863 (2016) 2977.
[54] G.-Y. Liou, P. Storz, Free Radic. Res. 44 (2010) 479.